Astron. Astrophys. 317, 328–349 (1997)

ASTRONOMY
AND
ASTROPHYSICS

ROSAT PSPC survey of M 31⋆

R. Supper[1], **G. Hasinger**[1,2], **W. Pietsch**[1], **J. Trümper**[1], **A. Jain**[3], **E.A. Magnier**[4,5], **W.H.G. Lewin**[4], **and J. van Paradijs**[5,6]

[1] Max-Planck-Institut für extraterrestrische Physik, Postfach 1603, D-85740 Garching, Germany
[2] Astrophysikalisches Institut, An der Sternwarte 16, D-14482 Potsdam, Germany
[3] QAD Isro Satellite Center, Airportroad, Bangalore 560017, India
[4] CSR and Department of Physics, Massachusetts Institute of Technology, Room 37-627, Cambridge, MA 02139, USA
[5] Astronomical Institute "Anton Pannekoek", University of Amsterdam, Kruislaan 403, 1098 SJ Amsterdam, The Netherlands
[6] Physics Department, University of Alabama in Huntsville, Huntsville, AL 35899, USA

Received 24 February 1995 / Accepted 13 January 1996

Abstract. This paper reports on results of the analysis of the first M 31 survey with the ROSAT PSPC performed in July 1991. Within the ≈ 6.3 deg^2 field of view we detected 396 individual X-ray sources with (0.1 keV – 2.4 keV) fluxes ranging from $\approx 5 \times 10^{-15}$ erg cm^{-2} sec^{-1} to $\approx 4 \times 10^{-12}$ erg cm^{-2}sec^{-1}. Of these 396 sources, 43 have been tentatively identified with foreground stars, 29 with globular clusters, 17 with supernova remnants, 3 with other galaxies (including M 32), and 3 with radio sources. A detailed analysis of the integral flux distribution of the sources shows that approximately one fifth are likely to be background objects. By comparison with the results of the *Einstein* M 31 survey, we find 327 newly detected sources, 15 moderately variable sources, 3 bright and 6 faint possible transient sources. For those sources in M 31, the observed luminosities range from $\approx 3 \times 10^{35}$ erg sec^{-1} to $\approx 2 \times 10^{38}$ erg sec^{-1} (at 690 kpc). The total (0.1 keV – 2.4 keV) luminosity of M 31 is $(2.9 \pm 0.3) \times 10^{39}$ erg sec^{-1}, roughly one third of which is from the bulge and two thirds of which are from the disk. The luminosity of a diffuse component within the bulge region is estimated to be less than 3.2×10^{38} erg sec^{-1}. An explanation in terms of hot gaseous emission leads to a maximum total gas mass of $1.7 \times 10^6\ M_\odot$. We find that the integral luminosity distribution of sources associated with globular clusters is similar to that of the Milky Way. Finally, the results of spectral fits to 56 of the brightest sources are discussed; we classify 15 objects as "supersoft sources" according to their spectral characteristics.

Key words: galaxies: fundamental parameters – galaxies: individual: M 31 – galaxies: luminosity function – galaxies: spiral – X-rays: general – X-rays: stars

Send offprint requests to: R. Supper

⋆ Tables 5 to 9 are only available in electronic form (LaTeX-files) at the CDS via anonymous ftp 130.79.128.5.

1. Introduction

The giant early-type spiral galaxy M 31 is the most massive galaxy in the Local Group and is close enough for a detailed study of accreting X-ray sources with luminosities comparable to those in our own Galaxy. Using the *Einstein* Observatory, Trinchieri and Fabbiano (1991, hereafter TF) discovered 108 point sources in four IPC pointings, with a total of 100 kiloseconds of exposure, and several HRI pointings, with a total of more than 200 kiloseconds of exposure. Three IPC observations of ≈ 30 ksec each covered $\approx 86\%$ of the D_{25} diameter of M 31 (Tully 1988; D_{25} is defined as the galactocentric diameter of the 25 magnitude per arcsec^2 isophote in blue light) with a limiting sensitivity of approximately 10^{37} erg sec^{-1} for the distance of M 31 (van Speybroeck et al. 1979; van Speybroeck and Bechtold 1981; Long and van Speybroeck 1983). The IPC images contain various isolated sources in the outer portion of the galaxy and a confused region surrounding the nucleus. This central region was resolved into individual sources with the HRI on three occasions separated by 6 month intervals. Additional HRI followup observations for more than half of the IPC sources gave positions accurate to about $3''$. A comparison with optical and H I observations showed that there is a large group of X-ray sources associated with the bulge and a general association of X-ray sources with the spiral arms of the galaxy.

Crampton et al. (1984) found a variety of possible optical counterparts within the error circles of the source positions, including globular clusters, foreground stars, faint blue stars, and the compact galaxy M 32. Crowding in the optical nucleus prevented the examination of source positions within $2' - 3'$ of the center of the galaxy.

TF pointed out that the luminosity distribution of the disk sources in M 31 identified with *Einstein* is comparable with that of the bulge sources. They also noted a difference between the optical and the X-ray brightness profiles of M 31. Primini et al. (1993), using ROSAT HRI data, reported that X-ray luminous

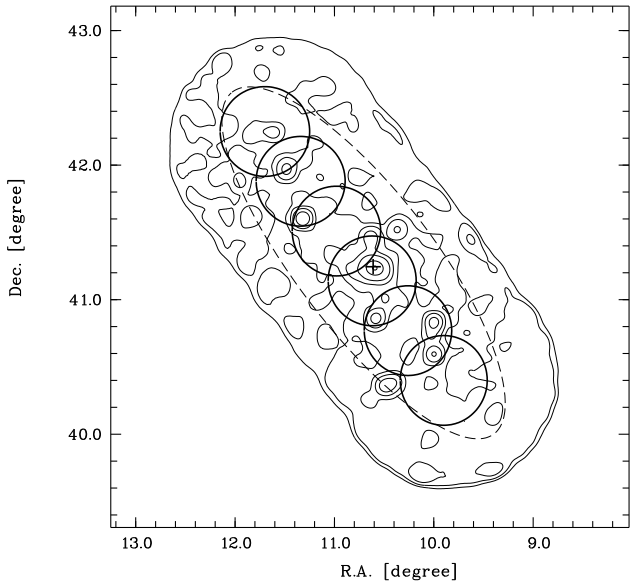

Fig. 1. Locations of the central regions (with 20′radii) of the 6 survey pointings (thick circles) and the D_{25} ellipse of M 31 (Tully 1988; dashed ellipse), plotted over a contour plot of M 31 (0.5 - 2.0 keV). The thick cross marks the optical center of the galaxy.

globular clusters are more numerous in M 31 than in our Galaxy by a factor of 4, although the peak luminosities are comparable.

The first ROSAT PSPC deep survey of M 31 discussed in this paper covered the whole galaxy (1.3 times the D_{25} diameter) with a total observation time of more than 200 kiloseconds, leading to a sensitivity which is about a factor 10 greater than that of the *Einstein* observations. In total, 396 sources were found in the ROSAT PSPC survey of M 31. In this paper, we present a complete catalog of these sources, report on the initial results of optical identifications and discuss their X-ray spectral properties. The luminosity distribution of these sources, the fraction of background sources, and the luminosity distribution of X-ray sources correlated with globular clusters are presented.

2. Observations

The analysis in this paper is based on the pointed M 31 survey with the ROSAT X-ray Telescope Position Sensitive Proportional Counter (ROSAT PSPC; Trümper 1983, Aschenbach 1988, Pfeffermann et al. 1986) performed in July 1991. The results of a second PSPC survey of M 31 carried out in August 1992 will be reported elsewhere. An isolated observation of the bulge region of M 31 was performed in July 1990 with the ROSAT High Resolution Imager (HRI), and has been described by Primini et al. (1993).

The July 1991 M 31 survey consisted of 6 contiguous pointings, each with more than 25 000 seconds observation time, covering the whole disk at equally spaced positions. The observations were performed in the fixed pointing mode, because the normal ROSAT wobble mode could not been used due to temporary difficulties with the attitude control system after the loss of a gyro. The journal of observations is given in Table 1. Fig. 1 shows an overlay of the central regions of the 6 pointings and the D_{25} ellipse of M 31 (Tully 1988) on the ROSAT X-ray (0.5 - 2.0 keV) contour plot of M 31. Each circle marks the boundary of the inner field of the PSPC with 20′ radius, where the instrument has the highest angular resolution: 20″ at 1 keV (Hasinger et al. 1992). When merged, these inner regions cover a large fraction of the D_{25} ellipse. The cross marks the optical center of the galaxy. The total field of view of the PSPC is 57′ in radius, and is approximately represented by the outer contour line.

3. Analysis

In most of the analysis, the individual pointings were treated separately, as explained below. For investigations of single sources (particularly for spectral fits) the data were taken from the pointing in which the source appears at the smallest detector off-axis angle which is free from shadowing by the rib structure of the PSPC entrance window. In contrast, for the investigation of the total X-ray luminosity of M 31 and its distribution, all pointings were merged into a single image.

3.1. Energy bands, images, and contour maps

The ROSAT XRT covers a broad energy range from 0.1 keV to 2.4 keV, hereafter called the 'B' band. To make use of the energy resolution of the ROSAT PSPC (Pfeffermann et al., 1986), we divided the broad energy band (B) into three energy ranges: a soft band (S: 0.1 keV - 0.4 keV) and two hard bands (H1: 0.5 keV - 0.9 keV; H2: 0.9 keV - 2.0 keV; with H: 0.5 keV - 2.0 keV = H1 + H2).

Fig. 2 shows a mosaic of the B-band data from all 6 pointings with pixels rebinned to $26'' \times 26''$. The individual pointings are evident via the shadows of the PSPC support structure. Since the bulge region is serverely crowded, we binned the data in this region at a higher resolution ($5'' \times 5''$ pixels) using only the H-band, which has the narrowest point spread function (PSF; Hasinger et al. 1992). The result is shown in Fig. 3 as a contour plot. The crosses mark the positions of the sources detected within this region, as described in Sect. 3.3. As seen in this figure, the bulge consists of single bright sources embedded in a region of diffuse emission which is likely to be due to a combination of unresolved point sources and/or hot gas emission.

3.2. Source detection strategy

The Extended Scientific Analysis System (EXSAS; Zimmermann et al. 1993) was used for the analysis of all 6 observations. The source detection was carried out separately for each pointing, using the following procedure:

First, the data were binned into images for each of the five energy bands B, S, H1, H2, and H with a pixel size of $15'' \times 15''$. For each of these 5 images, a 'local detection algorithm' was used, in which a 3×3 pixel box was moved across the image, looking for a significant excess within the box compared

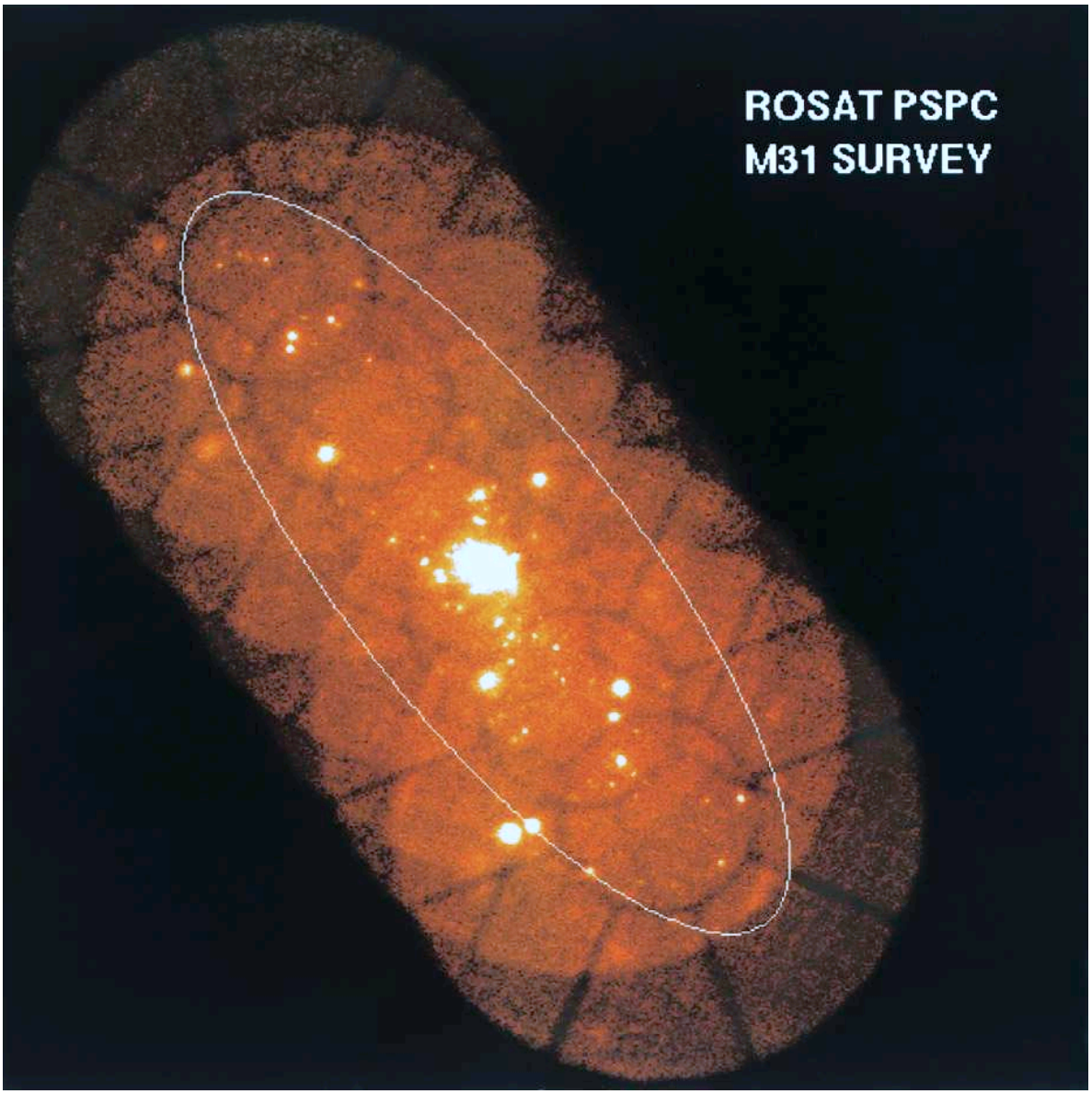

Fig. 2. Overlay of all 6 ROSAT PSPC pointings of M 31. The rib-structure of the PSPC entrance window can clearly be seen as shadows in each of the single images. The ellipse shows the D_{25} size of M 31.

to the background in the surrounding 16 pixels. We define the likelihood L = -ln(P), where P is the probability that the measured number of photons in the 3×3 pixel box originates from Possonian background fluctuations. For this step, a likelihood threshold of 8 was choosen. The result is a list of possible source positions, the "local detection list", for each of the 5 energy bands. Using this detection list, background maps were created as follows: first the images were smoothed by a Gaussian filter with $\sigma = 1$ pixel. Next, holes with a radius of 8 times that of the PSF were punched at the positions of the sources in the local detection list. The pixel values in the holes were replaced by the average value of the pixels surrounding the holes. Finally, the images were again smoothed with a Gaussian filter, this time with a σ equal to the on-axis σ of the PSF for the given energy band.

In the next step, a 'map detection algorithm' was performed with the background images and the original images. A 3×3 pixel box was again moved across the image, looking for significant excess within the box, but this time, the background was determined from the equivalent position on the background image. Again, likelihood threshold of 8 was chosen. This process yielded an additional position list, the "map detection list", for each of the 5 energy bands. The local and the map detection lists for each energy band were then merged and used as input for the maximum likelihood algorithm described by Cruddace et al. (1988). The maximum likelihood algorithm was performed on the original (i.e., unbinned) data, using the background im-

Table 1. Log of the first ROSAT PSPC survey of M 31.

Pointing	Date	RA (J2000)[1]			Dec (J2000)[1]			Exposure
		(h)	(m)	(s)	(°)	(′)	(″)	(s)
WG600065P	24.-25. July 1991	00	46	48.0	42	15	00	26 216
WG600066P	25.-26. July 1991	00	45	21.6	41	52	48	30 720
WG600067P	26.-27. July 1991	00	43	55.2	41	30	36	27 884
WG600068P	27.-28. July 1991	00	42	28.7	41	08	24	28 888
WG600064P	15.-16. July 1991	00	41	02.4	40	46	12	49 292
WG600079P	14.-15. July 1991	00	39	36.0	40	24	00	42 188

[1]The coordinates give the center of the field of view.

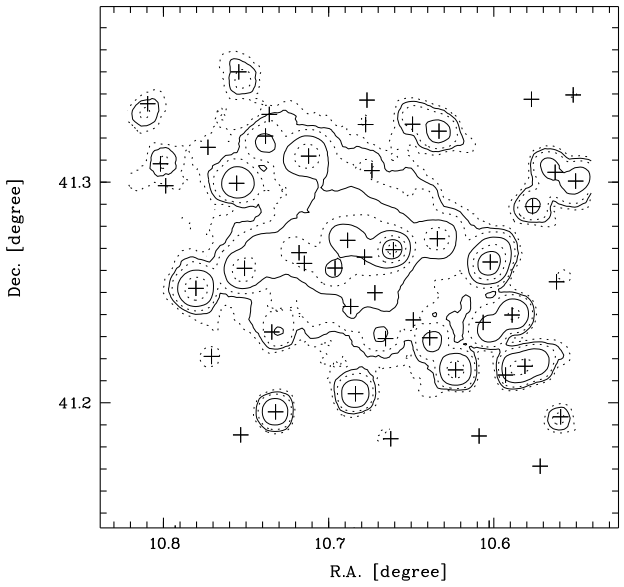

Fig. 3. Contour plot of the bulge region of M 31 in the hard energy band; X-ray point sources found with ROSAT within this region are marked as crosses. The contour levels are: 8.4, 11.7, 16.7, 33.4, 83.6, 167.2, 334.5, 501.7, and 668.9 cts s^{-1} deg^{-2}. The few sources not surrounded by any contour line are faint or soft objects.

ages described above, to yield the final positions of the sources, their extent and the corresponding statistical errors in position and extent. Only sources with a likelihood ≥ 10 were accepted. After this procedure the lists for the 5 different energy bands in each of the 6 pointings (i.e. 30 source lists) were merged into one unique source position list by combining sources when their 2σ positional uncertainties or their 2σ circles of the PSF overlapped spatially. In such a case, the position with the highest likelihood was maintained.

After the automatic merging procedure we visually inspected the results. The merging algorithm merged source #208 with source #210 (see Table 5). The visual check led us to the conclusion that these sources should *not* be merged because of different spectral characteristics. It should also be mentioned that the determination of a source position by the maximum likelihood algorithm can be biased by nearby sources, i.e. the position tends to shift towards the nearby source.

Finally, this list was used to perform a maximum likelihood calculation with fixed source positions, in order to compute the count rates in each of the five energy bands. In the case of non-detection of a faint source in one of the energy bands, we computed the 1σ upper limit on the flux in that energy band.

3.3. General properties of the detected X-ray sources

The source detection algorithm yielded 396 X-ray sources. The spatial distribution is shown in Fig. 4, in which they are plotted on an optical image of M 31, taken from the photographic O–plate of the Palomar Observatory Sky Survey. The different symbols and colors indicate roughly the X-ray flux of the sources: green circles – $F < 10^{-14}$, blue circles – $10^{-14} \leq F < 10^{-13}$, green crosses – $10^{-13} \leq F < 10^{-12}$, and blue crosses – $F \geq 10^{-12}$ erg sec^{-1}Cm. These fluxes were calculated using the count rates in the B-band given by the maximum likelihood algorithm, assuming a power law spectrum with $\Gamma = -2.0$ and $N_H = 9 \times 10^{20}$ cm^{-2}. A closer look at the bulge region is shown in Fig. 3. Because of the high density of sources found in this region, this area is shown as a contour plot; the crosses mark the positions of all sources detected within this area.

Table 5 lists the data for all 396 sources. Column 1 gives our source number, column 2 - 7 list the centroid position (epoch J2000) after correction for a systematic offset (see Sect. 4) and column 8 shows the 1σ uncertainty of the source position in arcsec. The calculation of this positional uncertainty is based on the maximum likelihood algorithm and incorporates the effects of statistical errors depending on the number of source counts, as well as the blur radius of the PSF at the off-axis angle and mean photon energy of the source. We also set a minimum threshold of $5''$ to account for a systematic position error. Any boresight correction considering a possible rotation of the separate pointings against each other was neglected (we found this error to be less than $\sim 7''$). The parameter in column 9 represents a classification of the quality of the detection. The sources in the first class were detected in the central region of the PSPC with off-axis angles $\leq 20'$, the second class defines locations of sources found between $20'$ and $40'$, and the third class contains sources with off-axis angles $> 40'$. As already mentioned in Sect. 2, we derived the source position from the pointing in which it appears at lowest off-axis angle, i.e., the best class (but not under a PSPC rib). Column 10 gives the highest likelihood of existence

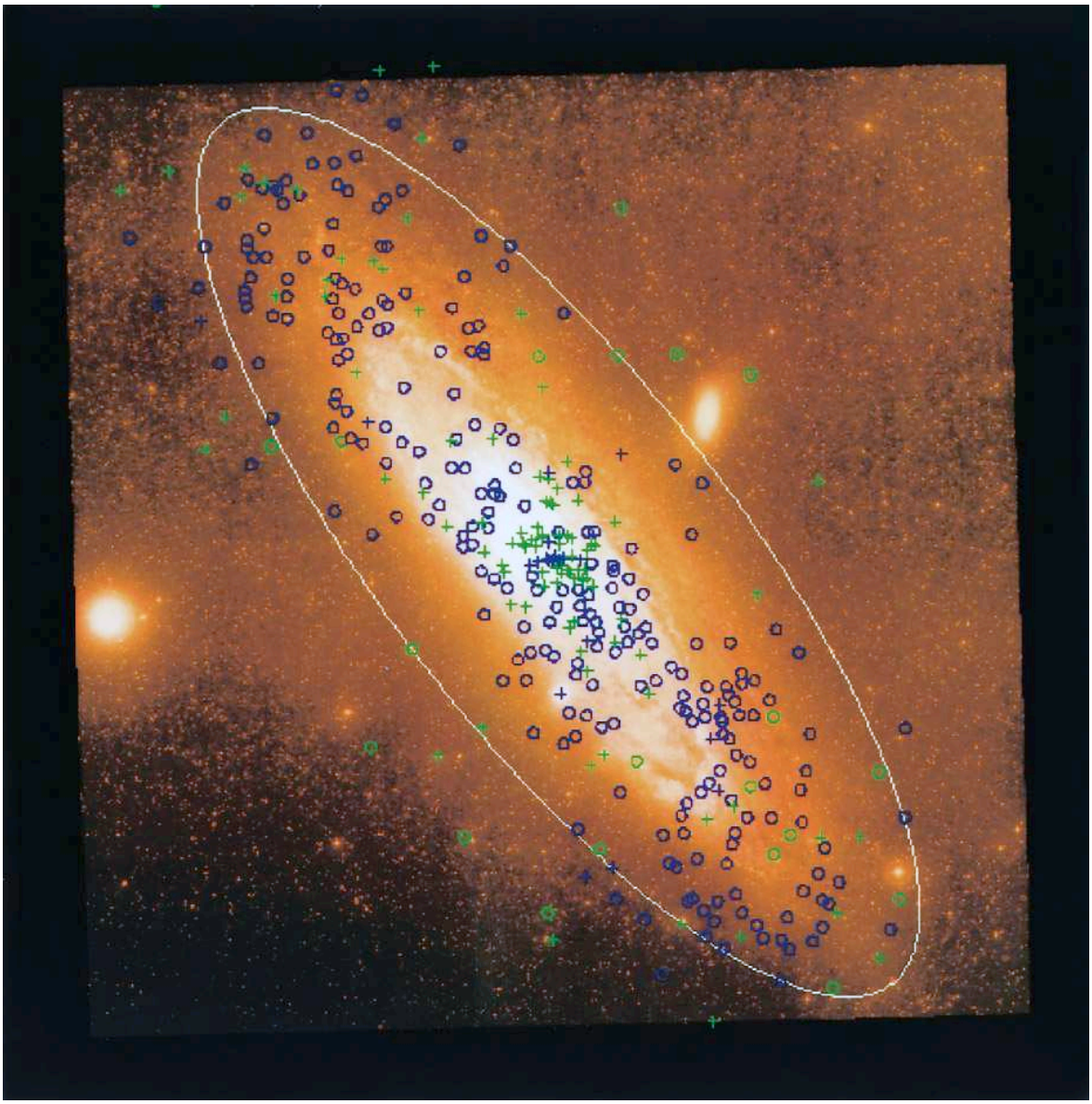

Fig. 4. Plot of all X-ray sources detected by the ROSAT PSPC overlayed over an optical image of M 31. The different symbols and colors correspond to the flux of the sources (see text). The ellipse indicates the D_{25} size of M 31.

found in any of the five energy bands (the energy band with the significant detection is indicated by the letter behind the likelihood value) computed with the maximum likelihood method. Columns 11 to 15 list the count rates with their 1σ error (in counts per kilosecond) within the five energy bands (B, S, H, H1, and H2; see Sect. 3.1). The listed count rate errors are only statistical errors, whereas the systematical errors are expected to be less than $\pm 15\%$. Because some faint sources were not detected in all energy bands (i.e., these sources had a likelihood below the threshold value of 10 in the energy band without detection), we present the 1σ upper limits for their count rates. The upper limits are computed from the 1σ fluctuation (poissonian statistics) of the background counts at the source position and are indicated by a preceding '<'-symbol in Table 5. For class 2 and especially class 3 sources this upper limit can even be underestimated due to the wider PSF and the therefore higher possibility of rib influencies.

It is important to point out several caveats. The count rates for sources in the bulge region may be mis-estimated due to the high confusion. Frequently this leads to an overestimate. Counts from the diffuse emission or from neighbouring sources may be assigned to the wrong sources, causing errors in the measured count rate. Also, two or more sources may be blended into a single source. The confusion also influences the spectral characteristic of a source (i.e. the split up of the count rates into the different energy bands). For most of the sources in the bulge, the latter effect will not be so severe since, except for sources #181 and #208, they all have similar spectral characteristics.

Another problem arises in the comparison between count rates measured in the different energy bands. For 4 sources, the count rate given for the B-band is significantly lower than that of the sum of the $S + H$-band, and this is also the case for 13 sources when comparing their H-band count rates with that of the sum of $H1 + H2$. This is partly due to the fact that the reported errors are statistical errors and do not include systematic errors. The opposite situation where the count rate of the common energy band is significantly higher than the sum of the count rates in the single energy bands may also occur for the same reason (in fact it is the case for 10 sources considering the B-band and for 8 sources considering the H-band). Additionally, for the B-band exists the second reason of $B \neq S + H$. Finally, 30 sources are marked with a †-symbol in Table 5 to indicate problems in deriving their count rates. These problems are due to several disturbances like the poorly known PSF at high off-axis angles, the situation of the source within a confused region, or the influence of a PSPC rib in the neighbourhood of the source.

By folding the PSF with a Gaussian source model, the maximum likelihood algorithm determines the likelihood of any possible extent of a source ('extent likelihood'), and the implied radius of extent defined as the Gaussian parameter. Because of systematic errors connected with the approximative description of the PSF, strong point sources also appear as extended. Therefore care must be taken in evaluating the validity of any source extent determined with the maximum likelihood algorithm. We have found that none of the 396 ROSAT sources can be clearly identified having extended structure larger than 25″. This size corresponds to a linear dimension of $\sim 80pc$ (at the distance of M 31), comparable to the shells and the supergiant shell seen in the LMC and reported to have luminosities in the order of 10^{37} erg s^{-1} (Meaburn 1980, Trümper et al. 1991, Bomans et al. 1994).

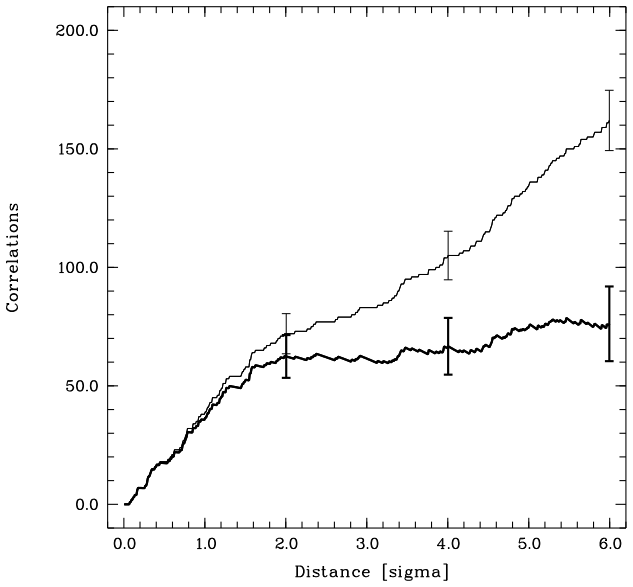

Fig. 5. Correlation of the ROSAT sources with the *Einstein* sources. It shows the number of correlations against the accepted correlation distance in units of σ of the combined positional error. The thin line shows N_{total} which represents the number of all possible correlations, whereas the thick line shows N_{excess}, which is N_{total} reduced by the statistically expected number of accidental correlations. For an explanation of the correlation process see text. The error bars give the 1σ errors.

4. Comparisons with other source catalogs

The 396 source positions were correlated with different published catalogs. In order to carry out these correlations, any systematic offset in the source list had to be determined. For the correlation technique only a brief description will be given here: Two catalogs will be correlated by calculating the distances in right ascension (δRA) and declination (δDEC) between every source in the first catalog and every source in the second catalog. If both catalogs contain identical source positions the values of δRA and δDEC will be zero for all matches, or distributed around (0,0) in the $\delta RA - \delta DEC$ plane if both catalogs have individual position errors. The number of uncorrelated coincidences can be calculated (see below). A mean nonzero value for the matching correlations gives a systematic offset between both catalogs.

To this end we looked for matching source positions of the globular cluster lists within an search-circle of 60″ radius around each ROSAT source. The reasons for the use of the globular cluster lists are their high position accuracy (1″) combined with the relatively large number of matches. To determine any systematic offset, δRA and δDEC were separately binned into histograms and fitted with a Gaussian distribution function. The mean of the Gaussian distribution function yields an offset of +5.1″ in RA and −9.4″ in DEC. This correction was applied to the raw position data to obtain the final source positions of the 396 X-ray sources which are listed in Table 5.

The corrected source positions were correlated with the catalogs listed in Table 2 and described in Sect. 4.2. Because the maximum likelihood algorithm yields statistical position errors for each source, these errors should be considered in the correlation method. Therefore, a technique has been used, in which the distance between two sources was calculated in units of their combined position errors (expressed in σ). Analogous to the technique explained above the pairs with distances between 10σ and 15σ were used to evaluate an accidental correlation rate n per σ^2. In order to derive the real correlations, only distances up to 2σ were accepted. This method yields the number of total correlations (N_{total}), the number of accidental correlations ($N_{acc.} = 4\pi n$), and the number of real correlations ($N_{excess} = N_{total} - N_{acc.}$). A representative example can be seen in Fig. 5, where the results of the correlation with the *Einstein* source list of TF is plotted as a cumulative distribution function. The thick line shows N_{excess}, the thin line N_{total}, and the error bars represent the 1σ errors.

Table 2 summarizes the results of this correlation analysis for different catalogs; these are discussed in more detail in the following subsections.

Table 2. Summary of the correlation analysis. N_{total} gives the number of all possible correlations within a distance of 2σ of the combined positional error, $N_{acc.}$ gives the number of statistically expected accidental correlations, and $N_{exc.}$ gives the excess of correlations, which is $N_{total} - N_{acc.}$. The final accepted correlations are somewhat less. For a detailed explanation see Sect. 4.2.

Type	Data bases	N_{total}	$N_{acc.}$	$N_{exc.}$
X-ray	*Einstein* (TF)	72	9.5	62.5
GC	BA87, BA93, MA94a	31	7.3	23.7
Extragalactic	NED	6	0.2	5.8
Foreground	MA92, SIMBAD	51	24.3	26.7
SNR	DO80, BW93, MA94b	22	4.9	17.1
Novae	SA91, SA92	0	0.6	–

4.1. Comparison to the Einstein sources

The ROSAT PSPC observations reveal many more sources in the disk regions of M 31 (i.e., outside the bulge) than were found in the *Einstein* observations (341 vs. 58). This is a result of both the $\sim$ 10 times higher sensitivity of ROSAT as well as the more complete coverage of the field of M 31. In contrast, the ROSAT PSPC data for the bulge region (within 5′ of the core) reveal only 22 sources compared with the 48 found in the *Einstein* HRI observations and the 45 found with the ROSAT HRI observations. This difference can be attributed to the reduced resolution of the ROSAT PSPC compared with either the *Einstein* or ROSAT HRI detectors.

The source list of TF, containing 108 X-ray sources, was used to correlate our sources with those of *Einstein*. Because TF give no information about the positional errors of their sources, we used the general values reported by Crampton et al. (1984): 3″ for the 81 *Einstein* HRI positions and 45″ for the 27 *Einstein* IPC positions.

Accepting source distances up to twice the combined position error (2σ), N_{total} = 72 correlations with a probable contamination of $N_{acc.}$ = 9.5 accidentals were found (see Fig. 5). The individual correlations are listed in Table 6. Column 1 gives the ROSAT source number (ref. Table 5), column 2 the fluxes and 1σ errors of the ROSAT sources using the spectral model of TF (thermal bremsstrahlung with kT = 5 keV and $N_H = 7 \times 10^{20}$ cm^{-2} in the 0.2-4.0 keV energy band), column 3 lists the *Einstein* source numbers (ref. Table 2A of TF), column 4 the fluxes and 1σ errors given by TF, columns 5 and 6 the distances between the ROSAT source positions and the *Einstein* source positions in arcsec and in units of their combined position errors (σ) respectively. The last column shows the ratio between the fluxes obtained with ROSAT and *Einstein* and can be considered as a long term variability check between the epoch of the two observations.

Four ROSAT sources (#173, #200, #201, and #240) correlate with two different *Einstein* sources each, whereas 4 *Einstein* sources (#2, #10, #37, and #104) correlate with two ROSAT sources each, and *Einstein* sources #70 and #88 with three ROSAT sources each. Although ROSAT source #67 correlates with *Einstein* source #3 only within 4.3σ error radius, we additionally accept this correlation pair because the source is one of the 30 critical sources mentioned in Sect. 3.3, and the poorly-known PSF uncertains the position for this very bright source. A check by eye confirms that the two sources are the same. Of the 108 *Einstein* sources, 43 could not be correlated to any ROSAT source, while 327 of the 396 ROSAT sources could not be correlated to any *Einstein* source.

Table 3. List of variable X-ray sources. F_R gives the ROSAT source flux using the *Einstein* spectral model of TF and F_E gives the *Einstein* source flux of the correlated *Einstein* source. The two undefined upper limits for F_R are due to confused regions. Column "$S(F_R - F_E)$" lists the significance of the variability as described in text. A "T" in column "$S(F_R - F_E)$" indicates bright transients or possible faint transients when enclosed in brackets (see Sect. 4.1 for a detailed explanation).

ROSAT Src.	F_R ($\times 10^{13}$) (cgs)	Einst. Src.	F_E ($\times 10^{13}$) (cgs)	F_R/F_E	$S(F_R - F_E)$
57	0.12 ± 0.05	2	1.64 ± 0.42	0.07 ± 0.04	3.56
69	19.87 ± 0.29		<?	>?	T
122	12.98 ± 0.45	9	8.72 ± 1.08	1.49 ± 0.19	3.65
150	9.32 ± 0.31	16	3.88 ± 0.75	2.40 ± 0.47	6.74
159	35.67 ± 0.32	15	48.83 ± 1.61	0.73 ± 0.02	8.02
172	5.78 ± 0.24	27	3.38 ± 0.52	1.71 ± 0.27	4.16
175	3.23 ± 0.19	33	0.83 ± 0.28	3.89 ± 1.33	7.09
188	31.65 ± 0.52	51	9.16 ± 1.01	3.46 ± 0.39	19.80
195	4.04 ± 0.21	58	1.59 ± 0.44	2.54 ± 0.72	5.06
205	18.21 ± 0.44	67	11.95 ± 1.10	1.52 ± 0.15	5.27
206	9.47 ± 0.32	68	5.64 ± 0.58	1.68 ± 0.18	5.81
211	2.44 ± 0.18	70	3.77 ± 0.34	0.65 ± 0.08	3.43
217	3.58 ± 0.21	76	1.64 ± 0.46	2.18 ± 0.63	3.82
220	8.77 ± 0.30	79	3.26 ± 0.42	2.69 ± 0.36	10.66
223	6.05 ± 0.26	80	1.92 ± 0.35	3.15 ± 0.59	9.44
348	5.39 ± 0.26	104	8.56 ± 0.48	0.63 ± 0.05	5.79
	<?	31	8.90 ± 0.65	<?	T
	< 0.06	40	1.59 ± 0.62	< 0.04	(T)
	<?	56	9.07 ± 0.64	<?	T
	< 0.14	81	1.04 ± 0.42	< 0.13	(T)
	< 0.37	93	2.86 ± 0.74	< 0.13	(T)
	< 0.13	96	3.50 ± 0.94	< 0.04	(T)
	< 0.05	100	0.71 ± 0.23	< 0.07	(T)
	< 0.10	106	0.71 ± 0.22	< 0.14	(T)

To measure the significance of the flux variability, we calculated the expression $S(F_R - F_E) = |F_R - F_E|/(\sigma^2_{F_R} + \sigma^2_{F_E})^{\frac{1}{2}}$ (Primini et al. 1993). Because this neglects a possible systematic error due to inaccuracies in our spectral model, we only accepted variability with a significance $\geq 3\sigma$. We also excluded bulge sources and other confused sources (such as ROSAT sources #340/#348, *Einstein* source #104) because of their large systematic errors. We found 15 potentially variable sources, listed in Table 3, where column 1 lists the ROSAT source numbers, column 2 the derived ROSAT flux (using the spectral model of TF), column 3 the correlated *Einstein* source numbers with their fluxes in column 4, column 5 the flux ratio (ROSAT / *Einstein*), and finally in column 6 the variability significance $S(F_R - F_E)$ derived with the formula given above.

Collura et al. (1990) report two variable sources among the sources detected with the *Einstein* satellite. The first, their source #4I, correlates with ROSAT source #150 which we also identify as variable between the *Einstein* and ROSAT observation. Collura et al. give for the logarithm of the luminosity (assuming power law spectrum with $\Gamma = -1.5$, $N_H = 3 \times 10^{20}$ cm^{-2},

0.2 - 4.0 keV, and 730 kpc for M 31 distance) a value of 37.6. Applying their spectral model to ROSAT source #150 yields for Log(L) a value of 37.7. This value lies within the variability range for the luminosity of $(16 \pm 3)\%$ reported by Collura et al. We confirm their identification of their source 4I as a globular cluster (ROSAT source #150, see Sect. 4.2).

The second variable source reported by Collura et al. is source 25I, which correlates with ROSAT source #316. In this case, we have no indication for time variability when comparing the ROSAT source flux with the *Einstein* source flux using the spectral model of TF. Applying the spectral model of Collura et. al. to ROSAT source #316 yields Log(L) = 37.4, whereas Collura et al. reports Log(L) = 37.2, which would indicate a variability in luminosity of $\sim 60\%$. Collura et al. report an effective amplitude of $(14 \pm 2)\%$ with a time scale of $> 10\,000$ seconds (observation I575), and $(40 \pm 6)\%$ with a time scale $> 7\,000$ seconds (observation H4483).

We have also included bright transients in the list of variable sources. We define bright transients as those sources which are found in one catalog, and are bright enough to be detected in the other, but which were not seen. ROSAT sources with fluxes $\geq 10^{-12}$ erg cm^{-2} s^{-1} (applying the spectral model of TF) should have been seen during the *Einstein* observations. Conversely, *Einstein* sources with fluxes $\geq 10^{-12}$ erg cm^{-2} s^{-1} should have been seen in the ROSAT pointed survey, even when they are observed at high off-axis angles. Because of the confusion problems, we have excluded the bulge sources in this search for transients.

Using these criteria, we have identified 3 bright transients (see Table 3). Of the 327 ROSAT sources not detected with *Einstein*, only one, source #69, is found to be a bright transient. This source, with a luminosity of 1.1×10^{38} erg s^{-1}, apparently went into outburst just before the first ROSAT PSPC survey of M 31, because it was not seen during the ROSAT all sky survey 6 months before (which had a limiting X-ray luminosity of $\sim 2 \times 10^{37}$ erg s^{-1}; Kahabka et al. 1991) and later faded from view (additional pointed PSPC observation; Hasinger, private communication). We performed optical observations of the error box of this source on Aug 6, 1991, within 1 month of the ROSAT observations of the transient. These observations consisted of *BVRI* CCD images taken at the Michigan-Dartmouth-MIT 1.3m McGraw-Hill telescope. Each exposure was 600 seconds long. These images showed three stars within $10''$ of the location of the transient, and a fourth within $20''$. All four of these stars were visible in observations made in Sept 1990 (see the catalog of Magnier et al. 1992), and had magnitudes in the range 20.1 – 20.4. None had substantially different magnitudes in the Aug 1991 observations. Low resolution (≈ 3Å) spectra were obtained (kindly provided by Dr. Phil Charles) on Aug 18, 1991 with the La Palma 4.2m William Herschel Telescope using the ISIS spectrograph. For these spectra, exposure times of 2000 seconds were used. None of the stars in question showed signs of Hα emission lines. The two most likely types of bright transients which we expected were 1) a Be transient and 2) a soft X-ray transient. Given the lack of Hα emission lines from any of these stars, we conclude that this event was a soft X-ray transient. In such systems, the absolute optical magnitudes at the peak of the outburst are typically ≈ 0, implying an apparent V magnitude of ≈ 24, and the source would be somewhat fainter even 1 month after the outburst. Thus it is not surprising that we did not detect the system in our optical images. Most of the remaining 326 noncorrelated ROSAT sources have fluxes below the detection threshold of the *Einstein* IPC and therefore no statement can be made about any possible transient nature.

Two of the sources detected with *Einstein* are found to be bright transients. The remaining 41 uncorrelated *Einstein* sources have luminosities below the bright transient threshold mentioned above. Even though these 41 *Einstein* sources have luminosities above the detection threshold of the pointed ROSAT survey, they cannot all be considered as (faint) transients: 35 of these 41 *Einstein* sources lie within or nearby the bulge region and therefore are excluded because of possible confusion. The remaining 6 *Einstein* sources can be considered as possible faint transients (see Table 3).

We give upper limits for the fluxes of all transients listed in Table 3. For the two bright transients seen with *Einstein* but not with ROSAT, we cannot give any reliable upper limit for the ROSAT X-ray flux because both sources lie in confused regions. For the one bright transient seen with ROSAT but not with *Einstein*, we are not able to calculate an upper limit, because we do not know about the limiting sensitivity in flux of the *Einstein* observations in this region.

4.2. Identifications with optical and radio sources

To identify and classify individual sources, the ROSAT source list was correlated with the following public data bases and catalogs:

- **globular clusters:** the two lists of Battistini et al. (1987, 1993; hereafter BA87, BA93) and the lists of Magnier et al. (1994a; Table 2; hereafter MA94a),
- **extragalactic objects:** the NASA Extragalactic Database (version date: 30. Dec. 1992; hereafter NED),
- **foreground stars:** the catalog of stellar photometry described by Magnier et. al., (1992) and Haiman et al. (1994), hereafter MA92, and the SIMBAD catalog (Centre de Données astronomiques de Strasbourg; version date: Dec. 1989; hereafter SIMBAD),
- **supernova remnants:** the lists of d'Odorico et al. (1980; hereafter DO80), Braun & Walterbos (1993; hereafter BW93), and Magnier et al. (1994b; hereafter MA94b).
- **novae:** the two lists of Sharov and Alksnis (1991, 1992; hereafter SA91, SA92).

There exists some overlap between these lists and catalogs as we tried to incorporate all available data for each class of object.

Table 7 shows the result of the correlations. The columns are defined as follows:

Column 1: ROSAT source number (ref. Table 5).

Column 2: Correlated catalog. The abbreviations used are the same as defined above.

Columns 3+4: Distance between the ROSAT source position

and the correlated one in the catalog, in arcsec and in σ units, respectively. For the distance expressed in sigma the combined position error of the ROSAT source and the correlated catalog source was used.

Column 5: The name of the identified source as it is listed in the catalogs (for details see the remarks to the individual catalogs below).

Column 6: Type of the identified source. The used abbreviations mean: Galaxy = (background) Galaxy; GC = Globular cluster; Radio = Radio source; Star = Foreground star (with its spectral type in brackets, if available).

If two catalogs contain the same source (due to an overlap of the different catalogs) which correlates with one of the ROSAT sources, then the identifications of both entries are listed, separated by a comma in each column. If different sources in the catalogs correlate with one ROSAT source, then the catalog entries are listed one in each line behind the number of the ROSAT source. Some comments on the various catalogs and comparisons follow:

Globular Clusters: Battistini et al. (1987 and 1993) report errors in position of less than $1''$ for both lists (BA87, BA93). Magnier et al. (1994a) also give errors less than $1''$ (MA94a). For the correlations, the error of each source in these lists was fixed to $1''$. For all three lists the entry number in the considered list is given as an identification. As additional information, if available, the corresponding GC numbers from the catalogs of Sargent et al. (1977) and Crampton et al. (1985) are reported in brackets. Within the 2σ error level, we find N_{total} = 31 correlations, including 7.3 accidentals. ROSAT sources #73 and #282 correlate with two GCs each. Therefore, we identify 29 ROSAT sources with globular clusters.

Background Galaxies: Within the 2σ error level and using the NED catalog, we find N_{total} = 6 extragalactic identifications, including M 32. The number of accidentals is negligible.

Foreground Stars: The position accuracy in the MA92 survey containing foreground stars is better than $1''$. The index number of this catalog is given in the identification column for each correlating source. The SIMBAD database gives individual position errors for each listed source. Because objects other than foreground stars are listed with relatively large position errors within this database, only the foreground stars were used for the correlation with the ROSAT source list. As identification, the entries as listed in the SIMBAD catalog are given. In column 'Type' the spectral type of the foreground star is given in brackets if it is available. Altogether, within the 2σ error level, N_{total} = 51 correlations of ROSAT sources with foreground stars were found with 24.3 accidentals expected.

From *Einstein* and ROSAT medium and deep surveys we know the foreground source luminosity function. Using this distribution and taking into account the sensitivity of our observations, we find an upper limit of 54 foreground sources within the region covered by the MA92 survey, which does not cover the whole D_{25} ellipse of M 31. This value is in agreement with our correlation result. From the number of total foreground star correlations, we have removed 5 correlations: 2 foreground stars correlating with ROSAT source #218 because of the correlations of this source with a GC, which is in better agreement with its hardness ratios (see Sect. 5.2); 1 correlation of ROSAT source #220 for the same reason as for source #218; due to spectral properties described in Sect.+5.2 we reject 1 correlation of ROSAT source #258 with a foreground star which also correlates with a SNR of DO80; and 1 correlation of ROSAT source #188 with the SIMBAD foreground star $BD + 40\,147$ due to the relatively hard spectrum of this ROSAT source and its correlation in position with M 32 (for a further discussion of this matter see Sect. 5.4). The remaining 46 correlations are listed in Table 7. Within this list, ROSAT sources #8, #137, and #338 correlate with two different foreground stars each. Therefore, we identify 43 ROSAT sources with foreground stars.

Supernova Remnants: The SNR list of Braun & Walterbos (1993) contains individual position errors for each given SNR (BW93). D'Odorico et al. (1980) report general position errors of $8''$ in declination and $15''$ in right ascension (DO80). A total error of $12''$ was asssumed for the correlation process. For the position errors in the list of Magnier et al. (1994b) $1''$ was assumed (MA94b). Strictly speaking, MA94b is a collection of three individual lists containing strong SNR candidates based on H_α/S_{II} flux, weaker candidates based on this ratio, and candidates based on the absence of O/B type stars (for a detailed explanation see Magnier et al.; 1994b). For the identifications with the BW93 list, their identification entries are given in Table 7, for the DO80 list their entry numbers (followed, in brackets, by the corresponding numbers of the SNR lists of Baade & Arp (1964) and Pellet et al. (1978), if available), and for the MA94b list their source indices. Altogether, N_{total} = 22 correlations with SNRs (including $N_{acc.}$ = 4.9) were found. We rejected one correlation of ROSAT source #114 with a SNR because of the extremely soft spectrum (hardness ratios) of this source which identifies it as a "supersoft source" (see Sect. 5.3). ROSAT sources #116, #240, #262, and #274 correlate with two different SNRs each, and ROSAT sources #203 and #211 correlate with the same SNR. Unfortunately, these two sources have the same spectral properties (hardness ratios) and also their luminosities lie within the range for SNRs (e.g. Kahabka et al. 1993). Therefore, we consider both sources as X-ray emission from the SNR. This results in 17 identifications of ROSAT sources with SNRs. Their luminosities range from $\sim 10^{36}$ to $\sim 10^{37}$erg s^{-1}, when applying a thermal bremsstrahlung spectrum with $T = 10^7$K and $N_H = 6 \times 10^{20}$cm^{-2}.

Novae: The errors in position for the nova lists of Sharov and Alksnis (1991, 1992) are reported to be $1.3''$ and $3''$ respectively (SA91, SA92). Within the 2σ error level, no correlations with novae were found.

4.3. The luminosity function of the globular cluster sources

Of the 29 globular clusters sources we have identified with ROSAT sources, 27 are situated in the class 1 region of the pointed survey (i.e. the area covered by the inner $20'$ of the PSPC pointings). All 490 globular cluster candidates of MA94a also lie within the class 1 region, as well as 10 additional globular clusters from BA87 and BA93. The ROSAT detection threshold

within the class 1 region is 1.38×10^{-3}counts s^{-1}, which we take to be an upper limit on the flux of the 473 undetected globular clusters. Applying an exponential spectral model with kT = 5 keV in the 0.5 - 4.5 keV energy band and assuming 690 kpc for M 31 distance, the count rates can be converted to luminosities which can be compared with those reported by Hertz & Grindlay (1983) for Galactic globular clusters. We can determine the luminosity distribution of the 27 detected globular clusters within this region by using the Kaplan-Meier estimator to obtain a nonparametric estimate of the cumulative distribution function $\Phi(L)$ (Schmitt 1985). This distribution function $\Phi(L)$ gives the fraction of detected sources among all detectable sources at a given luminosity. The resulting distribution is shown in Fig. 6 (thick line). The equivalent distribution calculated for the Hertz & Grindlay (1983) observations of the Milky Way globular clusters is also shown (thin line). Both distributions are consistent with being from the same parent distribution: a Kolmogorov-Smirnov test yields a probability of 86% for this hypothesis. Furthermore, the maximum luminosities are comparable.

Earlier investigations (Battistini et al. 1982, Long and van Speybroeck 1983, Crampton et al. 1984 and references herein) reported a significant difference between both distributions and raised the question whether the globular cluster sources in M 31 are more luminous and/or more numerous compared with those in the Milky Way. Our analysis suggests that the fraction of X-ray bright clusters among the total cluster population in both galaxies is similar and also the maximum luminosity of X-ray bright globular clusters is comparable. This is the result of both, the more complete detection of X-ray luminous globular clusters with ROSAT and the also more complete list of the optical detected globular cluster population in M 31. However, as Magnier et al. (1994a) report, the total M 31 globular cluster population is somewhat uncertain. If the existing catalogs are still somewhat incomplete, the fraction of X-ray bright clusters in M 31 may be a bit lower than shown in Fig. 6 (factor ~ 0.85 on a logarithmic scale). On the other side, new investigations about the fraction of X-ray bright clusters in the Milky Way (Verbunt et al. 1995) also lowers the value for our Galaxy by approximately the same factor.

Applying a single power law $N(> L) = N_0 \cdot L^{\alpha}$ to the integral luminosity distribution of globular clusters in M 31, yields $\alpha = -0.63 \pm 0.04$ including all data points or $\alpha = -1.02 \pm 0.05$ when only considering luminosities $\geq 1 \times 10^{37}$ erg s^{-1}. The difference indicates a flattening of the distribution, quite comparable to the result of the Milky Way.

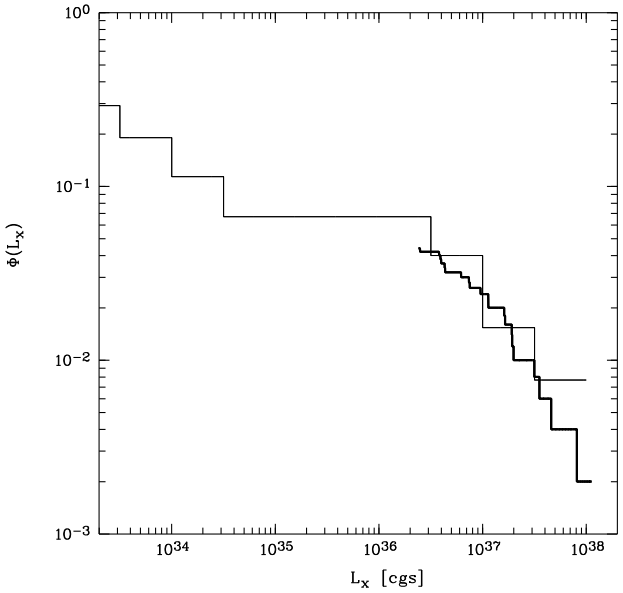

Fig. 6. The integral luminosity distribution of the globular cluster sources in M 31 (thick line) together with the distribution in our own galaxy (thin line) reported by Hertz and Grindlay (1983). Both presentations are normalized by the parameter-free estimator Φ described by Schmitt (1985; see also explanation in text).

5. Spectral properties

5.1. Spectral fits of bright X-ray sources

The energy resolution and sensitivity of the ROSAT PSPC enables us to derive spectral parameters for 56 of the brightest of the 396 detected sources, those detected with more than 200 counts by the maximum likelihood algorithm. Most of these 56 sources belong to the disk of M 31: although the bulge consists of very bright sources, most of them were omitted to avoid confusion problems. Since a detailed presentation of all 56 spectra is beyond the scope of this paper we quote the results of standard spectral fits using power law, thermal bremsstrahlung, black body, and thermal plasma (with solar abundancies) models. In addition we present a few representative spectra, including one for the bulge region in total (within $5'$ of the core).

To generate spectra, counts were integrated within a circle centered on the source position with a radius of 2σ of the 0.1 keV PSF. This region contains 95% of the total source counts in the S-band and $> 99\%$ of those in the H-band. The background spectrum was taken from an annulus around this source position from 2.5σ to 3.5σ of the PSF. In cases where this ring around the source was contaminated by photons of other sources in its neighbourhood, we took the background from another source-free region with comparable off-axis angle. A few sources with large distances to their neighbourhood sources allowed the collection of photons within a circle larger than 2σ to improve statistics. For these sources background photons were always taken from a ring between 0.5σ and 1.5σ of the PSF larger than the source photon collection circle. On the other hand for some sources, particularly in the bulge region, we were not able to include photons up to 2σ around the source position; in these cases, we limited the area to 1σ, corresponding to 68% of the source counts in the S-band and $> 95\%$ in the H-band. This limitation affects the resulting spectral fits in two ways. First, the computed luminosity is underestimated; although we applied a correction for the lost photons, the correction assumes an analytical (Gaussian) distribution function for the PSF which is only approximate. Second, the spectral hardness is overestimated, essentially for same reason: the PSF of the ROSAT PSPC

is energy dependent, with the greatest blur radius for the soft energy band (Hasinger et al., 1992).

The source and background counts were binned into spectra with a bin size chosen to provide a particular signal–to–noise ratio. For sources with more than 500 counts, the spectral bin width was chosen to give a signal–to–noise ratio of 5. For sources between 200 and 500 counts, the spectral bin width was chosen to yield a signal–to–noise ratio of 3. Various models for the spectral emission (power law, thermal bremsstrahlung, black body and/or Raymond-Smith thermal plasma – Raymond and Smith 1977) combined with interstellar absorption were fit to each spectrum in the energy range of 0.1 keV – 2.4 keV using χ^2 minimization. The fitted parameters included N_H, the total flux (0.1 - 2.4 keV), and either the spectral index (Γ) for the photon power-law model or kT for the thermal emission models.

The results of all fits are listed in Table 8. Column 1 gives the ROSAT source number, column 2 lists the photon collection radius in units of the PSF σ, and column 3 lists the number of photons which went into the fit. The next 9 columns are divided into three groups with three columns each. The first group contains the fitted parameter values for a power law model, the second group for a thermal bremsstrahlung model, and the third group for a black body or thermal plasma model respectively. There are 16 blank entries indicating that these fits did not converge for the given model or yielded unphysical results.

Table 9 lists the results of a power law fit with the N_H value fixed at 9×10^{20} cm^{-2}. This N_H values was chosen as it is the sum of the mean galactic foreground absorption (6×10^{20} cm^{-2} – Stark et al. 1991) and a mean effective absorption in M 31 (3×10^{20} cm^{-2} – Unwin 1980). The six sources identified as foreground stars (#8, #10, #95, #107, #135, #390) and the two galaxies (#134 and #188) contained in Table 8 are excluded in Table 9. The mean photon index of all sources in Table 9 is $\Gamma = -2.0 \pm 1.1$, and for the globular cluster sources alone $\Gamma = -1.6 \pm 0.3$. These errors are the 1σ value of an assumed Gaussian distribution, derived from the individual errors of the Γ_i, as described by Maccacaro et al. (1988).

To summarize the typical properties of several groups of sources, Fig. 7 shows a set of representative spectra:

Fig. 7a shows the spectrum of source #318, which is a bright **LMXB** located in a globular cluster. The measured N_H value of $(9 \pm 2) \times 10^{20}$ cm^{-2} (power law fit with free parameters; see Table 8) is consisent with M 31 membership. The spectrum is relatively hard ($\Gamma = -1.27 \pm 0.10$) compared to the average $\Gamma = -2.0 \pm 1.1$ for all sources or $\Gamma = -1.6 \pm 0.3$ for the average of all globular cluster sources. In addition, this source shows variability on a time scale of $\sim$ 16 hours (see Fig. 8a). The light curve was binned in intervalls of 402 seconds to prevent from influencies of a possible remaining wobble of the satellite.

Fig. 7b shows the spectrum and fit of a typical **foreground (flare) star**, here source #8. In addition to the fits in Table 8, a two-temperature thermal plasma model (Raymond-Smith) was also fit to this spectrum, yielding temperatures $kT_1 \sim 65$ eV and $kT_2 \sim 950$ eV and $N_H = 2.3 \times 10^{20}$ cm^{-2}, consistent with the galactic value. The light curve, binned in the same manner as described in case a) above, shows an outburst (increase in count rate by a factor of 10), representing a flare (see Fig. 8b). It should be noted that this source was identified as a foreground star on the basis of its X-ray spectral signature and the time variability of its light curve *before* the correlation with the foreground star list MA92 independently confirmed this identification.

Fig. 7c shows the spectrum and fit of one of the **Supersoft Sources (SSS)**, source #309, the brightest SSS we have found in M 31. One of the main characteristics of SSSs is their relatively high luminosity compared with their low temperature. A black body model fit yields $kT \sim 30$ eV, and a bolometric luminosity in the order of $\sim 10^{38}$ erg s^{-1}. Altogether, we have identified 15 SSS candidates in M 31. These sources are discussed in more detail below (Sect. 5.3).

Fig. 7d shows the spectrum of the **bulge region** in total and the fit with a thermal bremsstrahlung model. This fit yields temperature $kT \sim 1$ keV, and $N_H = (6.3 \pm 0.2) \times 10^{20}$ cm^{-2}. Because the temperature cannot accurately be determined, we calculate the total luminosity of the bulge with a typical temperature of $kT = 5$ keV. This model yields $L_{\mathrm{x,bulge}} \sim 1.3 \times 10^{39}$ erg s^{-1} (in the B-band).

Fig. 7e shows the spectrum of the source correlated with **M 32** (source #188). The fit is a thermal bremsstrahlung model (see Table 8) with a temperature of $kT \sim 2.6$ keV and $N_H \sim 7.8 \times 10^{20}$ cm^{-2}, yielding a luminosity of 1.9×10^{38} erg s^{-1}. For further discussion see Sect. 5.4.

5.2. Hardness ratios

Hardness ratios were computed for all 396 sources (or upper/lower limits), providing some spectral (color) information for the fainter sources which do not have enough photons to allow spectral fitting. Two different hardness ratios have been calculated, defined as: $HR_1 = (H - S)/(H + S)$ and $HR_2 = (H_2 - H_1)/(H_2 + H_1)$ (where S, H, H_1, and H_2 stands for the source counts in the considered energy bands calculated with the maximum likelihood algorithm). We use this spectral classification to investigate the source population of M 31. Typical HR_1 values for different source models and absorption columns are: $-0.6 \leq HR_1 \leq 0.1$ for thermal plasma with temperatures around $kT \sim 0.2$ keV and absorption of $N_H = (0 - 3) \times 10^{20}$ cm^{-2} (typical for foreground stars), $0 \leq HR_1 \leq 0.6$ for thermal bremsstrahlung with temperatures in a range of 0.2 - 0.5 keV and galactic absorption $N_H = 6 \times 10^{20}$ cm^{-2}, $0.7 \leq HR_1 \leq 0.9$ for power law with power index of $\Gamma \sim -2.0$ and absorption of $N_H = (6 - 10) \times 10^{20}$ cm^{-2}.

Fig. 9 shows histograms of the hardness ratios HR_1 and HR_2, as defined in Sect. 3.3. The HR_1 histogram demonstrates that most of the 396 X-ray sources have hard spectra (i.e. $0 < HR_1 \leq 1.0$). This is partly due to absorption along the line of sight, especially for the extragalactic background sources (see Sect. 6.2), and also to the relatively hard intrinsic spectra of X-ray binaries and AGN. There is also a distinct group of soft sources ($-1.0 \leq HR_1 < -0.5$) consisting mostly of foreground objects and the Supersoft Sources. More information about the sources with hard spectra can be obtained from

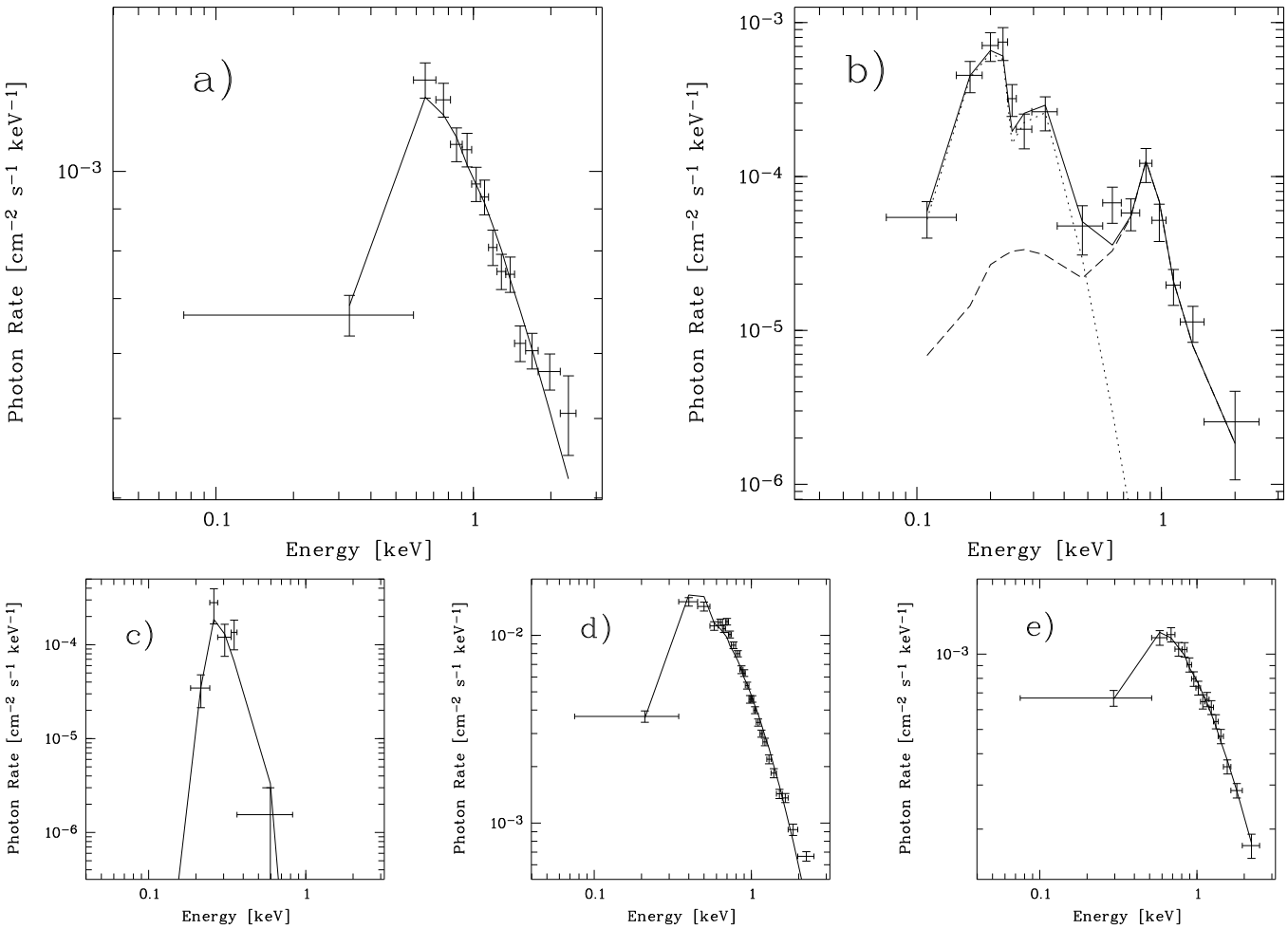

Fig. 7a–e. Five typical source spectra shown as measured photon rate against energy together with their best fits of a spectral model. **a** gives the spectrum of source #318, which is a bright LMXB located in a globular cluster. The best spectral model can be described by a power law with $N_H = (9 \pm 2) \times 10^{20}$ cm^{-2} and $\Gamma = -1.27 \pm 0.10$. **b** gives the spectrum of source #8, which can be identified as a foreground star. The spectral fit represents a two-temperature thermal plasma model with $kT_1 \sim 65$ eV and $kT_2 \sim 950$ eV together with $N_H = 2.3 \times 10^{20}$ cm^{-2}. **c** shows the spectrum of source #309, the brightest Supersoft Source in M 31. The drawn black body model fit yields a black body temperature of $kT \sim 30$ eV. **d** shows the spectrum of the bulge region of M 31. It can be well described by a thermal bremsstrahlung model with $kT \sim 1$ keV and $N_H = (6.3 \pm 0.2) \times 10^{20}$ cm^{-2}. **e** gives the spectrum of source #188, which correlates with the dwarf galaxy M 32. The drawn best fit is a thermal bremsstrahlung model which yields $kT \sim 2.6$ keV and $N_H \sim 7.8 \times 10^{20}$ cm^{-2}.

the HR_2 histogram. Fig. 9b shows a large group of "medium-hard" sources (around $HR_2 = 0.5$). From the definition of HR_2 it follows that, for sources with $HR_2 = 0.5$, the PSPC registers 75% of the counts in the high energy band (H_2) and 25% in the medium energy band (H_1). Applying the detector response, this hardness corresponds to temperatures between $kT = 1$ keV and $kT = 5$ keV.

The hardness ratio of the sources is plotted versus their B-band count rates in Figs. 10a and b. In the left hand panel of these figures, different symbols, listed in the lower right corner, have been used to mark the sources correlated with optical counterpart objects as well the Supersoft Sources (see Sects. 4.2 and 5.3). The hardness ratios errors are additionally encoded within the symbols: filled symbols represent errors ≤ 0.2, symbols with a dot in the center represent $0.2 <$ error ≤ 0.4, and empty symbols represent errors > 0.4. Furthermore, three representative error bars are shown. The right panel of these figures shows the unidentified sources, again with three representative error bars. From these figures it can be seen that the globular cluster sources and the SNRs are relatively hard, which is confirmed with spectral fits for the bright ones (Sect. 5.1). The (foreground) stars are more or less evenly distributed above and below a hardness of 0 for HR_1 and HR_2 (see below). Finally, all the Supersoft Sources have values near $HR_1 = -1$ due to the definition (see Sect. 5.3). In general, there is little correlation between the hardness ratios and the count rates, except for a general tendency for bright sources to be hard. In contrast, there is no tendency for faint sources to be soft. Faint sources (around 10^{-3} counts s^{-1}) are more or less uniformly distributed over the whole hardness ratio range.

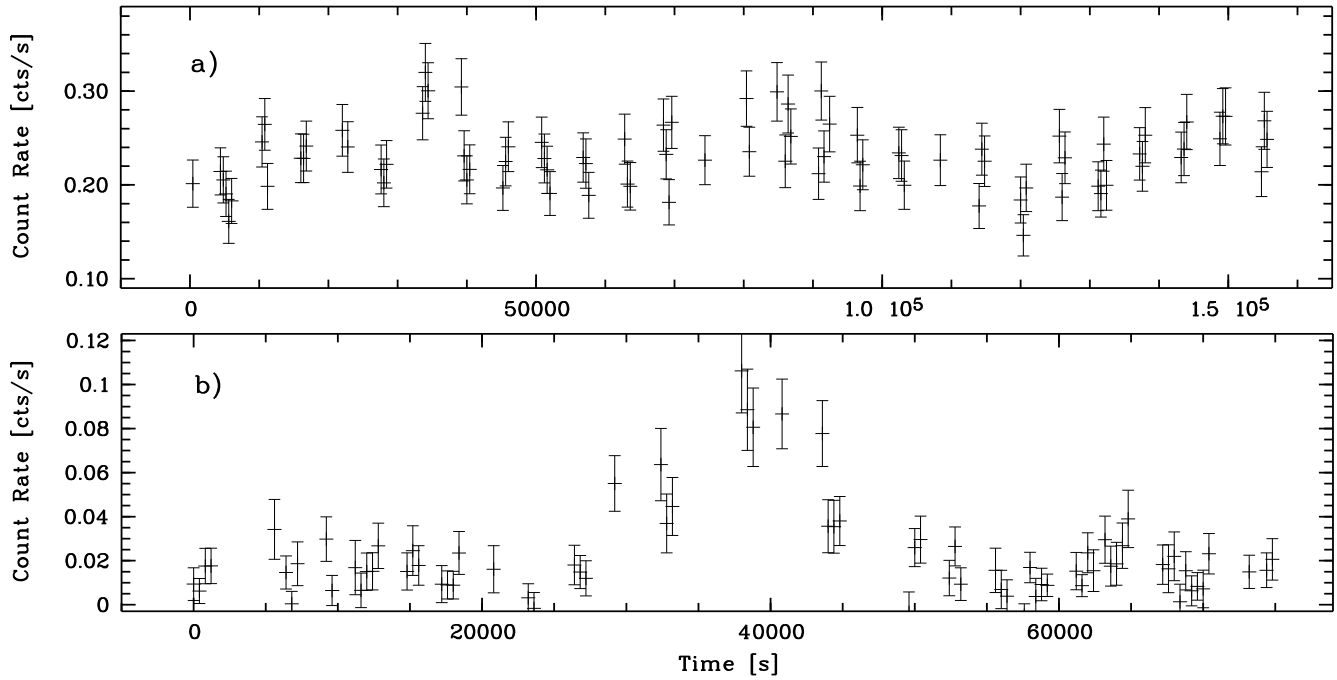

Fig. 8a and b. Two light curves of X-ray sources in M 31 showing variability: **a** gives the light curve of source #318 which correlates with a globular cluster and shows variability on a times scale of $\sim$ 16 hours; **b** gives the light curve of source #8 which was identified as a galactic foreground star. The increase in its count rate by a factor of 10 can be explained as a flare.

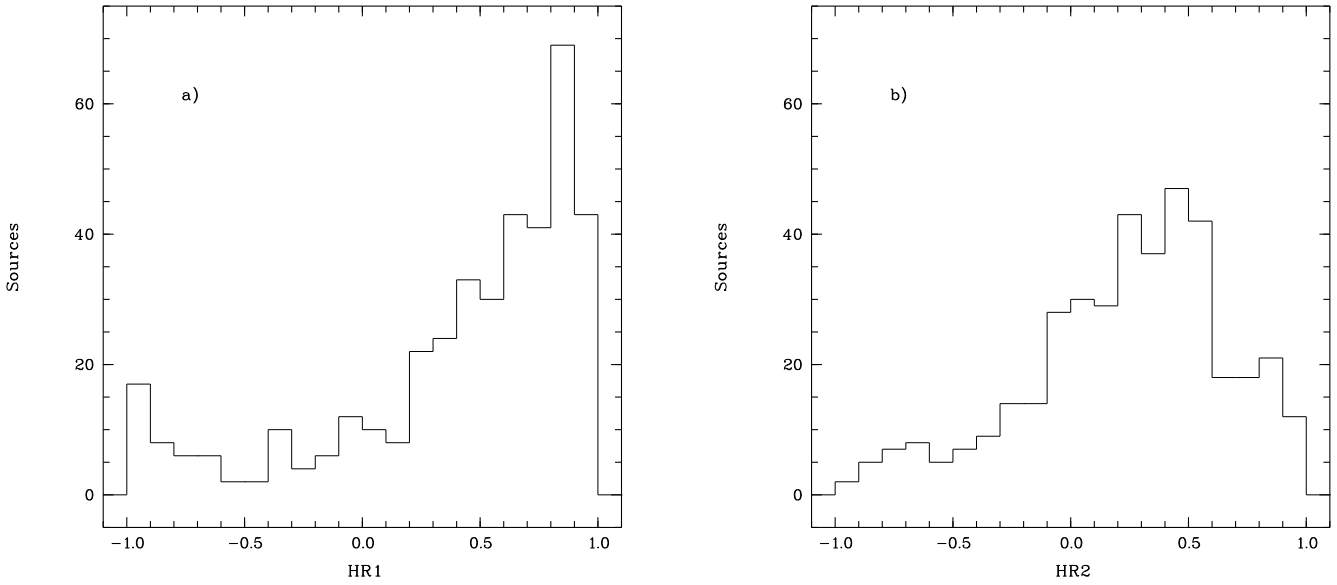

Fig. 9a and b. Histogram of the hardness ratio distribution: **a** HR_1; **b** HR_2.

Fig. 11 shows plots of HR_2 against HR_1, with Fig. 11a containing only identified sources and Fig. 11b containing the unidentified sources. The symbols in Fig. 11a are the same as for Fig. 10, without the representation of the errors. In both figures, the solid line indicates the relation expected for a power law model ($\Gamma = -2.0$) with a range of N_H values, from 2×10^{20} to 40×10^{20} cm^{-2}. Because HR_2 does not include the low energy band, which is strongly affected by N_H, the HR_2 values vary less than the HR_1 values for this range of absorption. Most sources are concentrated in the upper right quarter of the diagram, near the line of the spectral model and especially near the crosses for higher absorption values. This supports their identification as being extragalactic objects. As seen in Fig. 11a, all globular cluster sources and more than half of the SNRs are located in this quadrant. Of the foreground star sources, 18 also belong to this quarter of the diagram. Normally, foreground

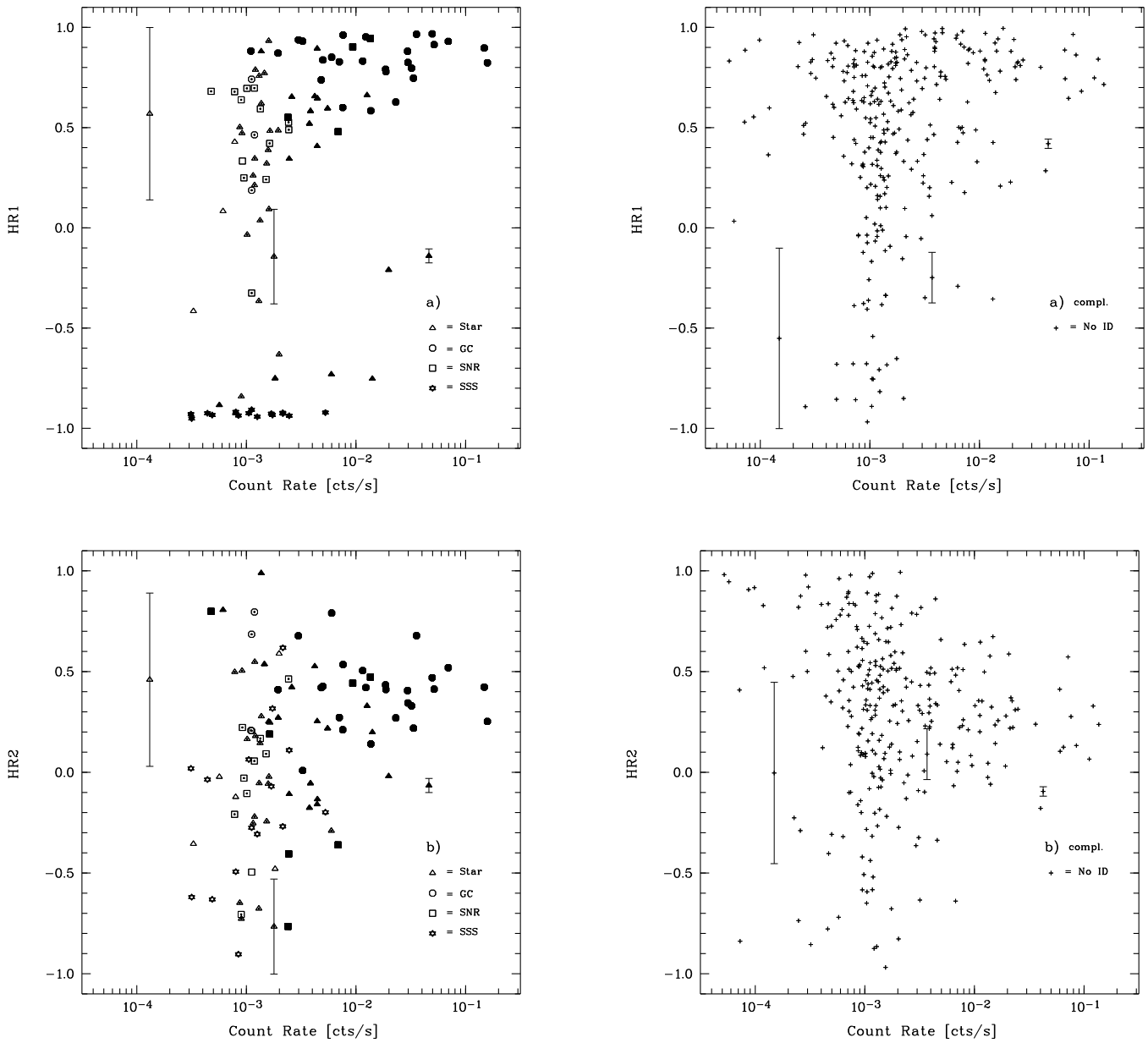

Fig. 10a and b. Hardness ratios plotted against the B-band count rates: **a** HR_1; **b** HR_2; each split into two diagrams with only the identified sources (plus the SSSs) on the left side and the unidentified sources on the right side. The different identifications are symbolized as the legend in the lower right corner shows. Three classes of hardness ratio errors are also encoded (empty, dotted, and filled symbols), as explained in Sect. 5.2, and representative errors for each class are shown.

sources would not be expected within this area and would refute the foreground hypothesis for these sources (they may represent the accidental correlations; see Sect. 4.2). But any intrinsic absorption in the low energy band of these sources is able to shift their hardness ratios and would explain their location in the upper right quarter of the diagram. Therefore, we decided to accept the results of the spatial correlation in Sect. 4.2.

In Sect. 4.2 source #258 was correlated to a SNR and also to a foreground star by spatial correlation. This source is too faint to allow a spectral fit, but the hardness ratios can help to find out the right correlation. A calculation of the mean value for HR_1 and HR_2 (using a method described by Maccacaro et al. (1988), assuming Gaussian distribution and using the individual errors of the HR_i) yields $HR_1 = 0.18 \pm 0.54$ and $HR_2 = 0.09 \pm 0.33$ for the X-ray sources correlated with foreground stars (without #258), and $HR_1 = 0.52 \pm 0.30$ and $HR_2 = -0.07 \pm 0.41$ for the sources correlated with the SNRs (also without #258). The hardness ratios of source #258 ($HR_1 = 0.70 \pm 0.39$, $HR_2 = -0.11 \pm 0.29$) agree better with SNR-values than with the values for the foreground stars. Because of

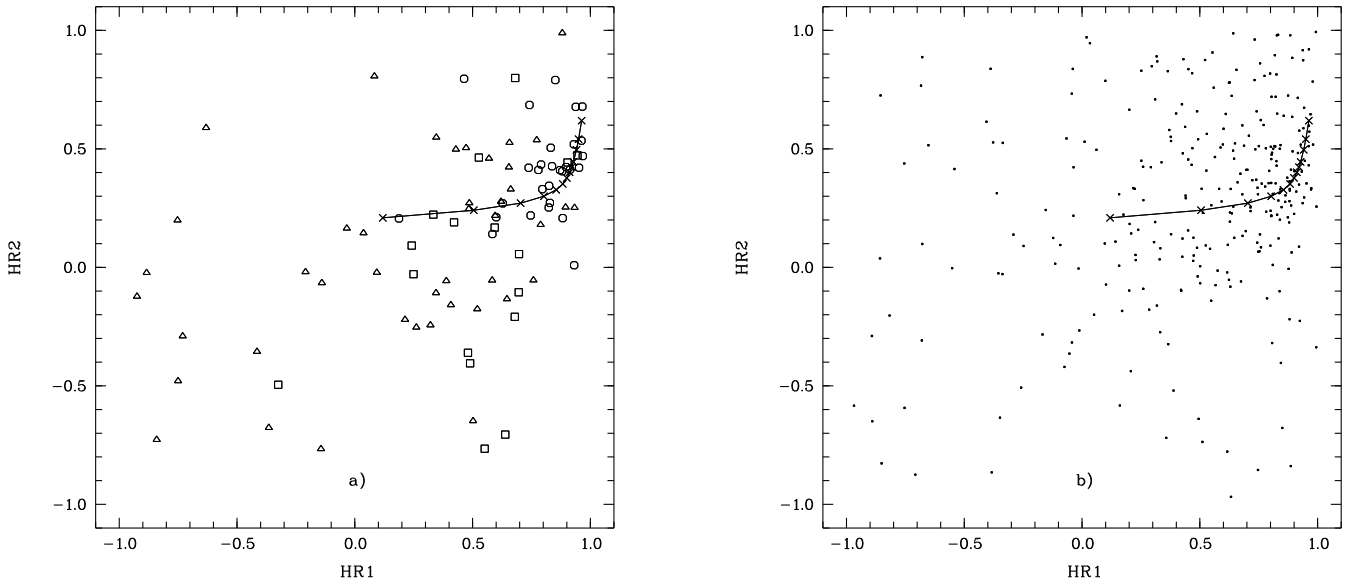

Fig. 11a and b. Diagram of HR_2 against HR_1. For the symbolization see legend of Fig. 10. In **a** the identified objects are plotted, in **b** the unidentified (drawn as dots). We also plot the theoretical points assuming a power law spectrum with $\Gamma = -2.0$ and for N_H values = 2, 4, 6, 8, 10, 12, 14, 16, 18, 20, 25, 30, and 40×10^{20} cm^{-2} (from left to right, marked with crosses and connected with a line).

the lack of other criteria we decided to reject the correlation of source #258 with a foreground star.

5.3. Supersoft sources

As already mentioned in Sect. 5.2, there exists a small group of sources having HR_1 values near -1, indicating that their spectra are very soft. Several of these sources have relatively high count rates, although the H I column absorbs the main part of their (soft) radiation. Because these objects could not be identified with foreground stars, they have to be considered as very soft but very luminous extragalactic sources. The criteria for selecting candidate SSSs are (see Hasinger 1994b): (i) $HR_1 + \sigma_{HR_1} \leq -0.80$ and (ii) the absence of correlation of the source with any known foreground object. The error in the hardness ratio ($\sigma_{HR_{1/2}}$) was calculated by applying Gaussian error propagation to the formular for $HR_{1/2}$. Among all 396 detected sources 15 fulfill this requirements: #3, #12, #18, #39, #78, #88, #114, #128, #171, #245, #268, #309, #335, #341, and #376. Only for source #309 the count rate is high enough, to apply a spectral fit, which yields a black body temperature of $\sim$ 30 eV, and a total luminosity of $\sim 10^{38}$ erg s^{-1} (see Sect. 5.1).

Several such "Supersoft Sources" (SSS) have been discovered with ROSAT (see Hasinger 1994a for a detailed review); they have been discussed by Greiner et al. (1991), Pakull (1989), Kahabka et al. (1994), Schaeidt et al. (1993), Trümper et al. (1991), and Wang & Wu (1992). The favourite explanation for these sources is in terms of white dwarfs in close binary systems accreting at a rate just sufficient for steady nuclear burning (Van den Heuvel et al. 1992).

5.4. M 32

Source #188 is coincident with the core of M 32, to within 10″. A thermal bremsstrahlung spectral fit yields a temperature $kT = (2.6 \pm^{0.4}_{0.6})$ keV (see Sect. 5.1 and Table 8). Fitting a power law to the spectrum of the source #188 yields $\Gamma = -1.8 \pm 0.1$, consistent with the globular cluster sources ($\Gamma = -1.6 \pm 0.3$). This source lies close to the center of M 32, has an X-ray luminosity of 1.9×10^{38} erg s^{-1} (690 kpc), and shows a variability of a factor of 3 (Table 3). We consider two possible descriptions of this source: 1) a superposition of several globular cluster sources in M 32 and 2) a "mini-AGN" black hole at the center of M 32 (Kormendy 1992). A followup HRI observation has been planned to determine the proximity between the source and the core of M 32 and also to check if this source can be decomposed into individual sources. For the time being we can conclude that the upper limit of the black hole luminosity is 1.9×10^{38} erg s^{-1} in the ROSAT B-band.

6. Background sources

Most of the 396 X-ray sources discovered with ROSAT in the field of M 31 have no optical or radio counterparts. In this section we estimate the fraction of extragalactic background sources in the sample. To do this, we use the results of the ROSAT deep surveys (Hasinger et al. 1993) and the X-ray absorption properties of M 31.

6.1. X-ray absorption properties of M 31

The photoelectric cross sections given by Morrison and McCammon (1983) and Balucinska-Church and McCammon (1992) were used for the calculation of the Galactic foreground

absorption. Because Morrison and McCammon determined the photoelectric cross sections for Galactic abundances (relative to the H I column density), we had to modify the calculations to the element abundances of M 31 when calculating the absorption within M 31 as follows: The abundances of the heavier elements have not been modified because the metallicity of M 31 does not differ significantly from that of the Milky Way (Blair et al. 1982). Koper et al. (1991) describe the CO surface brightness of M 31 being ~ 4 to ~ 6 times less than that of the Milky Way, but they argue that it is likely that the molecular mass is lower only by a factor of 2 for several reasons. Therefore, we used the half values of the galactic abundances for C and O. The H_2 molecular density in M 31 is reported to be 3 times less than the atomic H I density (Koper et al. 1991) and we considered this for the hydrogen abundancies. The uncertainty in the element abundances is estimated to $\sim$ 30%. Finally, it is known that there exist molecular clouds and local fluctuations in dust and CO in M 31. Although we do not know enough details about these variations, the CO clouds are reported to be apparently similar to those in the Milky Way (e.g. Boulanger et al. 1984).

To consider the spatial variation of X-ray absorption across M 31, the whole galaxy of M 31, defined by D_{25} = 193.2′ and d_{25} = 61.8′ as given by Tully (1988), was divided into 4 areas. The innermost is the bulge region: a circular area of radius 5′ (= 1 kpc) around the optical nucleus. The remaining three regions divide the disk of M 31 into regions according to their H I column density. The H I emission (Unwin 1980) is dominated by a ring-like structure at a galactocentric distance of $\sim$ 10 kpc within which the value of N_H rises up to $\sim 16 \times 10^{21}$ cm^{-2} in the line of sight.

We approximated this distribution by three elliptical disk annuli (see Fig. 12): The boundaries of the middle annulus (III) were chosen in such a way that within it the total (galactic and M 31) absorption is larger than 99.9% in the S-band. This corresponds to $N_H = 43.5 \times 10^{20}$ cm^{-2}. Annulus IV is then defined as the region between annulus III and the D_{25}-border of M 31, annulus II as the region between annulus III and the bulge region (I). Because of a slight asymetry of the H I structure with respect to the center of M 31, the annuli also are slightly displaced northeast. Table 4 lists each of the annuli, giving the displacement of the center along the semi-major axis, in kpc (column 2), the semi-major axis in kpc (column 3), the area in square degrees (column 4), the mean N_H in units of 10^{20} cm^{-2} (H I) along line of sight (column 5), and the resulting transmission in the H-band (column 6). The semi-minor axes are always taken be 0.32 times the semi-major axis (Tully 1988), and the position angle is 38°. The areas of these regions are large enough compared with local fluctuations of the H I distribution within M 31 that variations on the mean absorption will be statistically negligible.

Fig. 12 shows a sketch of these regions, numbered as in Table 4. The cross marks the optical center of the galaxy, the outer ellipse (border of area IV) is identical with the D_{25} ellipse of M 31. The envelope of the merged 6 pointings of the ROSAT PSPC survey of M 31 is also drawn in this figure.

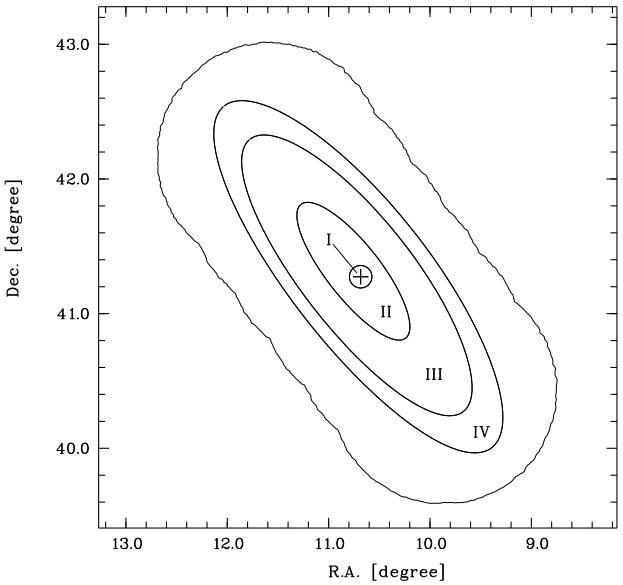

Fig. 12. Sketch of the elliptical annuli defined in Table 4. The envelope of the merged 6 pointings of the ROSAT PSPC survey of M 31 is also drawn. The cross marks the optical center of M 31.

Table 4. Characteristics of the X-ray absorption properties of M 31. Area I is a circle, whereas the areas II - IV are ellipses. See also Fig. 12. Column "a" gives the size of the major axis, "Area" list the area of the elliptic shells, "N_H" gives the mean absorption column of HI in M 31 as it results from the radio observations of Unwin (1980; i.e. without galactic absorption), and the last column gives the resulting transmission factor in the ROSAT H-band under consideration of galactic absorption.

Area No.	Center shift (kpc)	a (kpc)	Area (deg^2)	$\bar{N}_H$ (10^{20} cm^{-2})	Transm. H-band
I	0.0	1.0	0.026	7.9	0.798
II	0.8 to NE	7.6	0.384	11.1	0.654
III	0.2 to NE	15.4	1.274	77.0	0.260
IV	0.0	19.3	0.942	17.3	0.580

6.2. The fraction of background sources within the ROSAT PSPC source sample

We calculated an X-ray source count-rate distribution (logN-logS relation) for our source sample and compared it with known flux distributions of galactic foreground stars and extragalactic background sources to determine the fraction of non-M 31 sources in our sample. To facilitate a direct comparison with our logN-logS relation, the known logN-logS relations for the foreground and background sources must be folded with the detection conditions used to detect the X-ray sources of our source sample. This can be done in dividing these logN-logS relations by a sensitive area function which gives the variations of the sensitive survey area as a function of limiting flux.

In our case, these variations of the sensitive survey area are on one hand due to the different exposures of the individual

pointings, on the other hand due to the decrease in sensitivity within each pointing with increasing off-axis angles. Since we selected multiple-exposed source data from the most significant pointing (see Sect. 3.2) the final sensitive area is a complicated function of count rate. Additionally, the maximum likelihood algorithm used for the source detection was performed within each ROSAT energy band to maximize the number of detections. As an disadvantage this does not allow a direct computation of the count rate threshold for the logN-logS relation.

Therefore, for each of the 396 X-ray sources recalculations of the source count rates (within the H-band, i.e. 0.5 - 2.0 keV) and new likelihood values (NL) of source existence have been performed by using a more simple strategy. This strategy, explained in the following paragraph, allows the computation of the sensitive area function.

For this end, source counts in the 0.5 - 2.0 keV energy band were collected within 2σ of the PSF (0.5 keV) of the source position while the background counts were calculated from the background maps (computed as described in Sect. 3.2) for the same area. With these source and background counts a new likelihood (NL) for the existence of the source was calculated. For each source the values of the pointing with the highest NL were used for the logN-logS calculations. To obtain the accompanying sensitive area function the detection sensitivity across the survey area was calculated in steps of $45''$ by using the same procedure: at each position in the background map, the minimum detectable source count rate within a circle of 2σ of the PSF (0.5 keV) was calculated assuming a detection likelihood $NL \geq 10$, and taking into account the corresponding background count rate, vignetting and deadtime corrected exposure.

Using these detection thresholds, the total effective sky coverage within each of the annuli for a given source count rate was calculated. This function is shown in Fig. 13 for the D_{25} ellipse of M 31, and the elliptical areas III, IV, and II (going from top to bottom). The sensitive area for the D_{25} ellipse of M 31 is constant at 2.6 deg^2 down to count rates 4×10^{-3} cts s^{-1}. Between 4×10^{-3} cts s^{-1} and 1×10^{-3} cts s^{-1} the sensitive area decreases and drops down below 1×10^{-3}cts s^{-1}. The other three areas behave similarly with more or less earlier and steeper decrease below 1×10^{-3} cts s^{-1}. Their maximum sensitive areas are 1.259 deg^2, 0.944 deg^2, and 0.375 deg^2 for area III, IV and II respectively, which differs slightly from the theoretical areas listed in Table 4, because the square boxes of the $45''$-grid do not fill exactly the elliptic areas.

Because of consistency with the sensitive area function the following analysis had to be restricted to sources with NL $\geq$ 10, which results in a loss of 97 sources from among the 396 sources of the ROSAT source sample or a loss of 29 sources from among 328 sources of the ROSAT source sample detected in the H-band ($< 9\%$). On the other hand, additional sources would have been detected, if the strategy described above had been directly performed on the full data and not only at the source positions preselected by the maximum likelihood algorithm. An estimate revealed the latter to be less than the first. In summary, the uncertainty in the number of sources is of the order of a few percent. To check for the reliability of the following analysis, a second analysis had been calculated including only sources with NL $\geq$ 20 and using an accompanying sensitive area function. The results of both methods were comparable within the errors. Thus, we consider the fractions reported in Sect. 6.2.3 as valid for the whole source sample.

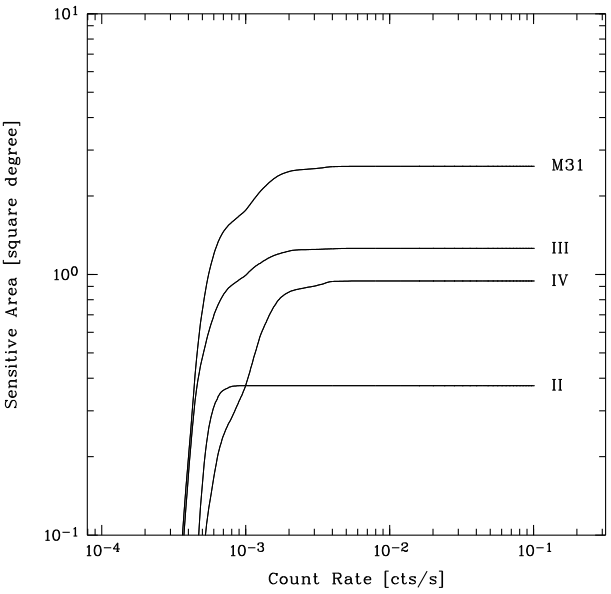

Fig. 13. The sensitive survey area as a function of limiting count rates for the D_{25} ellipse of M 31 and the three elliptical disk areas II, III, and IV.

6.2.1. The analytical logN-logS relation for foreground sources

We did not use the foreground stars identified in our own observations to calculate a logN-logS relaton for foreground stars because of the relatively large fraction of accidental correlations. Instead, we used the foreground star flux distributions from the *Einstein* and ROSAT medium and deep surveys (Hasinger 1995) which have a much larger sample. These data are well fit by a power law $N(> S) = k \times S^B$ with power index $B = -1.41 \pm 0.19$ (N expressed in sources per square degree) for fluxes down to 10^{-14} erg cm^{-2} s^{-1}. For an estimation of the number of foreground stars below 10^{-14} erg cm^{-2} s^{-1}, we extrapolated the fraction of foreground sources compared with the number of background sources (from the background logN-logS; see Sect. 6.2.2). Recent reports indicate, that this extrapolation leads to a slight overestimation of foreground sources (Jones et al. 1995). On the other hand, the sensitive survey area decreases dramatically below 10^{-14} erg cm^{-2} s^{-1} so that uncertainties of the foreground source distribution below this flux limit is increasingly negligible.

For the count rate to flux conversion a power law spectrum with $\Gamma = -2.0$ (the same used to compute the foreground star flux distribution function within Hasinger et al. 1993) and a mean galactic absorption of $N_H = 3 \times 10^{20}$ cm^{-2} was used (calculations with no foreground absorption leads to comparable results within the systematic errors of the whole procedure).

With this, the flux threshold of 10^{-14} erg cm^{-2} s^{-1} corresponds to $\sim 10^{-3}$ cts s^{-1}. Finally, applying the sensitive area as a function of limiting flux to the foreground logN-logS relation yields the predicted number of foreground stars within each area. The results will be presented in Sect. 6.2.3.

6.2.2. The analytical logN-logS relation for background sources

Because the logN-logS distribution for the X-ray background presented by Hasinger et al. (1993) is contaminated by foreground sources, the logN-logS relation for foreground stars (see Sect. 6.2.1) corrected to mean galactic absorption of $N_H = 3 \times 10^{20}$ cm^{-2} was subtracted first. Second, the resulting flux distribution was shifted towards lower fluxes according the extinction properties of M 31. This analysis was carried out separately for each of the annuli defined in Sect. 6.1. The transmission coefficients calculated from the average N_H values and listed in Table 4 were used to derive the shift to lower fluxes for the background logN-logS distribution. A power law spectral model was applied with $\Gamma = -2.0$ (Hasinger et al. 1993) to convert fluxes to count rates. Finally, the sensitive area as a function of the limiting count rate was applied to yield the number of predicted background sources in the different areas according to the observational properties of our M 31 survey (same procedure as already described above for the foreground source distribution).

6.2.3. Results of the analysis

The results of the background source analysis for the three disk areas are shown in Fig. 14 for the areas II, III, and IV respectively. In all three figures, the solid line shows the cumulative count rate distribution for all sources found with ROSAT within the considered area and with NL $\geq$ 10. The squared boxes represent the background sources predicted from the analytical distribution function reported by Hasinger et al. (1993; see Sect. 6.2.2). The error bars represent the uncertainties of the extinction properties of M 31 (see Sect. 6.1) together with the statistical errors of the background distribution. Finally, the triangles show the (foreground and background subtracted) source distribution of M 31 with errors as a result of the background distribution errors. It is common to all three figures that the slope of the cumulative count rate distribution for all sources (the upper graph) decreases when going from high to lower fluxes and flattens below 10^{-3} cts s^{-1}. This is mainly an effect of the decreasing sensitive area as shown in Fig. 13. The same happens to the predicted background source distribution function for the same reason. Therefore, as a result, this is also the case for the background subtracted distribution of sources belonging to M 31 (the triangles). We summarize the content of these diagrams as follows:

a) The cumulative background source distribution in area II reveals $\sim$ 20 sources down to our count rate limit and the foreground source distribution predicts $\sim$ 8 foreground sources (compatible with the 13 sources including 6 accidentals from individual correlations derived in Sect. 4). Therefore, from among 92 sources observed with NL $\geq$ 10 within this area $\sim$ 70% belong to M 31.

b) The cumulative source distribution for area III shows a much steeper slope near the count rate limit than for area II. Because area III is the one with the H I ring, the column density for absorption is so high, that not only a large fraction of the background sources are absorbed, but also a large fraction of the fainter sources of M 31 itself. The cumulation of the adjusted background source distribution yields $\sim$ 7 background sources at our count rate limit and the adjusted foreground source distribution predicts $\sim$ 22 foreground sources within area III (in agreement with the 18 sources including 9 accidentals found in this region by individual correlations described in Sect. 4). The total number of detected sources with NL $\geq$ 10 within this area is 99. Thus, $\sim$ 7% of all sources within this region are expected to be background objects, a consequence of the strong local extinction, and $\sim$ 70% are expected to belong to M 31.

c) The cumulative background source distribution in area IV reveals $\sim$ 18 sources at our count rate limit and the foreground source distribution predicts $\sim$ 9 foreground sources (comparable with the 11 sources including 5 accidentals found by correlations within this area). Therefore, from among 52 sources observed with NL $\geq$ 10 within this area $\sim$ 50% are expected to belong to M 31.

Because of the high uncertainty in fluxes of the bulge sources, due to confusion within this region, we do not compute a distribution function. Considering the larger number of sources found by Primini et al. (1993) with the ROSAT HRI within this region (45 sources compared to our 22 sources), it is a good approximation to accept all 22 sources as belonging to M 31.

In the region outside the D_{25} ellipse of M 31 where we have found 34 sources with NL $\geq$ 10, our analysis predicts 14 foreground sources. The remaining number of 20 sources is consistent with the predicted number of background sources. From the errors we expect less than 2 sources (1σ) as members of M 31.

In summary, we estimate that of all sources detected in our survey, $\sim$ 60% belong to M 31, $\sim$ 20% are foreground sources, and $\sim$ 20% are background objects (all three fractions with $\pm$10% uncertainty).

7. Total luminosity and diffuse emission

In this section we will use the term "diffuse component" to indicate the sum of the emissions from a truly diffuse (gaseous) emitter and from unresolved point sources. As "total emission" we will call the sum of the diffuse component and the emission from resolved point sources.

To investigate the total and partial X-ray luminosity of M 31 and a possible diffuse component, we tried to clean the observational data from contamination by particle background and solar X-ray scattering. Because the fraction of particle background drastically increases above a master veto rate of the ROSAT PSPC of 170 cts s^{-1} (Snowden et al. 1992), the data were selected for time intervals with master veto rates below this thresh-

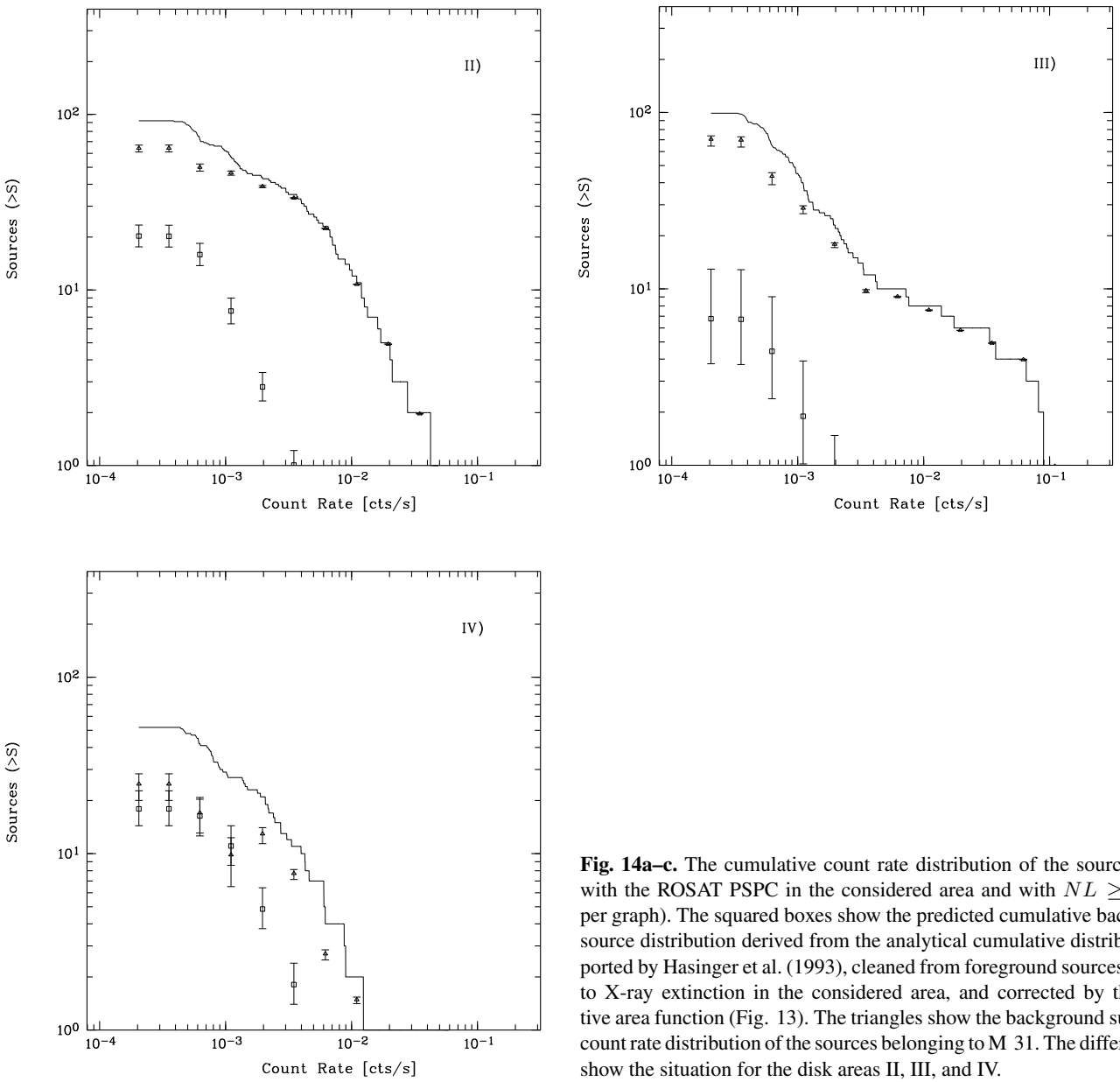

Fig. 14a–c. The cumulative count rate distribution of the sources found with the ROSAT PSPC in the considered area and with $NL \geq 10$ (upper graph). The squared boxes show the predicted cumulative background source distribution derived from the analytical cumulative distribution reported by Hasinger et al. (1993), cleaned from foreground sources, applied to X-ray extinction in the considered area, and corrected by the sensitive area function (Fig. 13). The triangles show the background subtracted count rate distribution of the sources belonging to M 31. The different plots show the situation for the disk areas II, III, and IV.

old. The fraction of solar scattered X-rays, which is produced by scattering of solar X-rays by oxygen in the higher atmosphere and therefore correlates with the iluminated oxygen column (Snowden et al., 1993), was reduced by selecting the data for an illuminated oxygen column of less than $10^{15}\mathrm{cm}^{-2}$. With these procedures the fraction of particle background and solar scattering could be reduced to $< 10\%$ for observations WG600065P, WG600066P, and WG600067P, and $< 6\%$, $< 1\%$, and $< 0.4\%$ for observations WG6000068P, WG600064P, and WG600079P, respectively (considering the B band).

These cleaned data were merged together and binned into an image with $30'' \times 30''$ pixel size. The resulting image was divided by an exposure map with the same pixel size to obtain a count rate image corrected for the effect of the rib structure, vignetting and dead time. This exposure map was calculated in the following manner: the B-band was divided into 10 energy slices for which EXSAS provides instrument maps for the PSPC detector response. Together with the photon event files, exposure maps for each of these energy slices were created additionally considering dead time effects. A weighted addition of these single exposure maps yields the final exposure map. The pulse height spectra in the 10 energy slices of the photon event files were used as the weighting factors.

The individual count rates in the four different areas defined in Sect. 6.1 (Table 4) were taken from this count rate image. "Background count rates" were taken from an area far outside and around the D_{25} ellipse of M 31 – explicitely the area between the ellipse with major and minor axes 0.15° larger than the D_{25} ellipse of M 31 and the ellipse 0.30° larger. We derived 41.19 ± 2.33, 5.44 ± 0.07, 4.17 ± 0.03,

and 3.76 ± 0.03 cts $s^{-1}deg^{-2}$ for area I, II, III, and IV respectively, and 3.65 ± 0.04 cts $s^{-1}deg^{-2}$ for the background count rate around the galaxy (the errors give the statistical error only).

Considering the bulge, a summation over the count rates of all 22 bulge sources detected in this area and listed in Table 5 yields (0.728 ± 0.004) cts s^{-1}. This corresponds to $(1.85 \pm 0.01) \times 10^{-11}$erg $cm^{-2}s^{-1}$ for the resolved flux in the B band when applying a power law as spectral model with $\Gamma = -2.0$ and $N_H = 6 \times 10^{20}cm^{-2}$ for galactic absorption. It yields $\sim 1.1 \times 10^{39}$erg s^{-1} in the B band for the luminosity of resolved bulge sources. For the total emission, the subtraction of the background count rate from the count rate derived in total in area I yields (37.5 ± 2.3) cts $s^{-1}deg^{-2}$. Multiplication with the bulge area of 0.026 deg^2 (Table 4) leads to (0.975 ± 0.060) cts s^{-1}, which is (0.247 ± 0.060) cts s^{-1} higher than the value for the resolved sources in this area mentioned above. This additional photon flux must be considered as the amount of a diffuse component. If we count these photons as completely originating from a gaseous emission, the application of a thermal bremsstrahlung spectrum with kT = 5 keV and $N_H = 6 \times 10^{20}$ cm^{-2} leads to a flux of $(4.6 \pm 1.1) \times 10^{-12}$ erg cm^{-2} s^{-1}, corresponding to a luminosity of $(2.6 \pm 0.6) \times 10^{38}$ erg s^{-1}. This would indicate a gas mass of $(1.4 \pm 0.3) \times 10^6$ $M_\odot$, assuming the gas fills uniformly the bulge region, a sphere with $5'$ radius (using the power per unit emission integral as a function of temperature for a low density plasma reported by Kato 1976). It is very likely that these photons not only originate from gaseous emission, but also from unresolved point sources, so that this gas mass is an upper limit.

Considering the disk, a summation over the count rates of all disk sources, i.e. sources lying in the areas II – IV, and listed in Table 5 yields (1.7 ± 0.1) cts s^{-1}. This corresponds to $(4.3 \pm 0.3) \times 10^{-11}$erg $cm^{-2}s^{-1}$ for the resolved flux in the B band when applying a power law as spectral model with $\Gamma = -2.0$ and $N_H = 6 \times 10^{20}cm^{-2}$ for galactic absorption. If we subtract the background count rate per square degree (derived from a region outside the D_{25} ellipse of M 31 as described above) from each of the count rates in the three areas and sum over the results after multiplication with the individual areas listed in Table 4, it yields (1.5 ± 0.1) cts s^{-1} for the disk count rate of M 31, which is (0.2 ± 0.14) cts s^{-1} lower than the value for the resolved sources in the disk of M 31 mentioned above. This slight difference, mainly introduced in the result by area III, may indicate a small amount of absorption of X-ray background radiation by the disk of M 31. This conclusion is supported by the fact that area III contains the largest column density of absorbing material (the area with the H I ring). A detailed discussion of absorption of M 31 will be the subject of a future paper. Within this paper we consider the just mentioned difference as negligible.

Because a fair amount of the detected sources do not belong to M 31, but are foreground sources or background sources shining through the galaxy, as already discussed in Sect. 6.2, the derived flux of all resolved disk sources mentioned above (or the sum of the flux in the three disk areas respectively) cannot be used for a determination of the total X-ray luminosity of the disk of M 31. To estimate the corrected value, we integrated the logN-logS distributions for the M 31 sources we have derived for each of the three disk areas in Sect. 6.2.3. Adding the results yields a total flux of $(3.2 \pm 0.5) \times 10^{-11}$ erg cm^{-2} s^{-1} for the disk of M 31 (using the spectral model mentioned above). This corresponds to a total luminosity of $(1.8 \pm 0.3) \times 10^{39}$ erg s^{-1}.

Comparison with the Einstein results:

Assuming a power law spectrum with $\Gamma = -2.0$, a foreground absorption of $N_H = 6 \times 10^{20}$ cm^{-2}, and a distance of 690 kpc for M 31 we found for the total B-band luminosity of M 31 $(2.9 \pm 0.3) \times 10^{39}$ erg s^{-1}. Using the *Einstein* observations, TF found a value of $\sim 3 \times 10^{39}$ erg s^{-1}. In comparing the two values, one has to take into account the different spectral models, energy ranges, and especially the different fields of M 31, investigated. TF derived the luminosities from the *Einstein* data by applying a thermal bremsstrahlung spectrum in the energy band 0.2 keV - 4.0 keV with kT = 5 keV and $N_H = 7 \times 10^{20}$ cm^{-2}. They integrated the count rates within an ellipse of $\sim 2.5^\circ \times 1.0^\circ$ which is a bit smaller than the D_{25} ellipse we used for our calculations. A conversion of our results to the spectral model of TF, would yield for the total luminosity $(3.0 \pm 0.3) \times 10^{39}$ erg s^{-1}. The perfect agreement with the value reported by TF, however, is somewhat accidental: while our observation covered the whole galaxy, those of TF did not. On the other hand, TF did not correct for background sources.

Comparing the luminosity of the bulge region, the ROSAT luminosity of $\sim 1.1 \times 10^{39}$ erg s^{-1} is lower than the value of 1.5×10^{39} erg s^{-1} TF reported for the *Einstein* observation (in this case the effect of the different spectral models – our's and TF's – is below the errors and therefore negligible). But TF did not give the value for the bulge, but only reported a "roughly equally division (of the luminosity) between bulge and disk". Additionally, we found a higher luminosity for the disk ($(1.9 \pm 0.3) \times 10^{39}$ erg s^{-1}, when converted to the *Einstein* model) than TF found. Therefore we cannot agree with the ratio of X-ray luminosity between bulge and disk TF reported. We find a ratio of 0.5 ($1/3$ from the bulge, $2/3$ from the disk).

Additionally, an indication for a diffuse emission in the bulge region was found. We derived an upper limit of $(2.6 \pm 0.6) \times 10^{38}$ erg s^{-1} for a diffuse component in the bulge region. TF report $\sim 3.8 \times 10^{38}$ erg s^{-1}, which is $(46 \pm 27)\%$ higher than our upper limit. Because TF did not report errors, we are not able to access the statistical significance of the difference. Furthermore, this may be a contribution due to systematic differences in the instruments and analysis methods. Another reason could be, that TF did not detect the slight indication of absorption of M 31. They used the area around the bulge as background (whereas the background in this paper was taken from around M 31), but this value could be too low, due to a possible absorption around the bulge and the fact of no significant absorption within the bulge region. In summary, we find that the discrepancy between the gas mass derived by TF of $\sim 2 \times 10^6$ $M_\odot$ (assuming the diffuse emission completely originates from gaseous emission) and our upper limit of $(1.4 \pm 0.3) \times 10^6$ $M_\odot$ does not represent a serious problem.

8. Summary and conclusions

The first pointed ROSAT PSPC survey of M 31 has led to the detection of 396 X-ray sources in the ~ 6.3 deg^2 field of view, 22 of them in the very confused bulge region. Their luminosities range from $\sim 10^{35}$erg s^{-1} to 3×10^{38}erg s^{-1}, assuming a distance of 690 kpc for M 31. Of these sources, 43 sources have been identified with known foreground stars, and 29 sources with globular clusters in M 31. We also found 17 identifications with SNRs, three radio sources, and three galaxies including M 32. A comparison with the *Einstein* source list reported by TF confirms 65 *Einstein* sources, 15 of which appear to be variable. Futhermore, six faint possible transients and three bright transients were discovered, of which one appears in the ROSAT observation and two in the *Einstein* observation. Finally, 43 of the *Einstein* sources were not detected in the ROSAT observations (including the transients), whereas 327 ROSAT sources were not seen during the *Einstein* observation.

The integral luminosity distribution of 27 globular cluster sources can be represented by a single power law with a power index of -0.63 ± 0.04, or -1.02 ± 0.05 if only globular cluster sources with luminosities $\geq 10^{37}$ erg s^{-1} are included. A comparison with the X-ray luminosity distribution for the globular clusters in our own galaxy leads to the conclusion that both come from the same parent distribution. This is against earlier reports, which described the luminosity distribution function of globular cluster sources in M 31 normalized to the known number of GCs as being higher compared to the Milky Way (Battistini et al. 1982, Long and van Speybroeck 1983, Crampton et al. 1984).

We have estimated the fraction of background sources within the ROSAT source sample by dividing the disk of M 31 into three regions with different mean H I column densities (according to radio measurements of Unwin (1980)) and comparing with the X-ray flux distribution function with that of the background sources reported by Hasinger et al. (1993). Accordingly, $\sim 70\%$ are expected to be sources in M 31, $\sim 20\%$ are expected to be background objects, while the rest of $\sim 20\%$ are expected to be foreground sources.

For the bulge region, we can give an upper limit to a diffuse component in the range of $(2.6 \pm 0.6) \times 10^{38}$ erg s^{-1}, which is a factor of ~ 1.5 lower than TF reported. If we count this luminosity as completely originating from hot gas (kT = 5 keV) within the bulge region, this would indicate a gas mass of $(1.4 \pm 0.3) \times 10^6\, M_\odot$ as an upper limit. For the total luminosity of M 31 we find $(2.9 \pm 0.3) \times 10^{39}$ erg s^{-1}, for the bulge alone 1.1×10^{39} erg s^{-1}. So, for the total luminosity we find a ratio between bulge and disk of 0.5 ($1/3$ from the bulge, $2/3$ from the disk), which differs from the *Einstein* observations, although the total is the same as TF reported.

We have studied the spectral energy distribution for 56 sources. The majority of the sources belonging to M 31 can be well described by a power law with $\Gamma = -2.0$ and $N_H = 9 \times 10^{20}$ cm^{-2} within the 0.1 - 2.4 keV energy band. Most of the sources have spectral properties comparable to those expected for accreting objects. One source, which correlates in position with the elliptical dwarf galaxy M 32 shows a relatively hard spectrum and a luminosity in the range of 10^{38} erg s^{-1}. This source may be associated with a central black hole believed to exist from observations of the stellar dynamics, but our observations do not exclude a superposition of binary X-ray sources.

We identify 15 sources with the new class of "Supersoft Sources". They show extremely soft spectra and no correlation to known foregound stars.

Finally we note that the 396 ROSAT sources found in the sky region of the Andromeda galaxy is higher than what was found with the UHURU satellite in the Milky Way and in the whole sky 20 years ago. The deep ROSAT observations of the local group galaxies now allow investigations of more detail than the UHURU survey did for our own Galaxy.

Acknowledgements. We thank the MPE ROSAT group for their support. Parts of our analysis used the SASS and EXSAS data analysis software. We would like to thank Phil Charles for obtaining WHT spectra of candidate counterparts to the transient source #69. We thank the referee for his very useful suggestions. We thank NASA and the Centre de Données astronomiques for the online access to their data bases. The ROSAT project has been supported by the Bundesministerium für Bildung, Wissenschaft, Forschung und Technologie (BMBF) and the Max-Planck-Gesellschaft (MPG). WHGL was supported by NASA Grant NAG5-1826. EAM acknowledges support by the Netherlands Foundation for Research in Astronomy (ASTRON) with financial aid from the Netherlands Organization for Scientific Research (NWO) under contract number 782-376-011.

References

Aschenbach B., 1988, Appl. Opt. 27, No. 8, 1404
Baade W., Arp H.C., 1964, ApJ, 139, 1027
Balucińska-Church M., McCammon D., 1992, ApJ 400, 699
Battistini P., Bònoli F., Buonanno R., Corsi C.E., Fusi Pecci F., 1982, A&A 113, 39
Battistini P.L., Bònoli F., Braccesi A., et al., 1987, A&AS 67, 447
Battistini P.L., Bònoli F., Casavecchia M., et al., 1993, A&A 272, 77
Blair W.P., Kirshner R.P., Chevalier R.A., 1982, ApJ 254, 50
Bomans D.J., Dennerl K., Kürster M., 1994, A&A 283, L21
Braun R., Walterbos R.A.M., 1993, A&AS 98, 327
Boulanger F., Bystedt J., Casoli F., Combes F., 1984, A&A 140, L5
Collura A., Reale F., Peres G., 1990, ApJ 356, 119
Crampton D., Cowley A.P., Hutchings J.B., Schade D.J., Speybroeck L.P.van, 1984, ApJ 284, 663
Crampton D., Cowley A.P., Schade D., Chayer P., 1985, ApJ 288, 494
Cruddace R.G., Hasinger G.R., Schmitt J.H., 1988, The Application of a Maximum Likelihood Analysis to Detection of Sources in the Rosat Data base. In: Murtagh F., Heck A. (eds.) Astronomy from Large Databases. ESO Conference and Workshop Proceedings No. 28, Garching/Germany, p. 177
D'Odorico S., Dopita M.A., Benevenuti P., 1980, A&AS 40, 67
Emerson D.T., 1976, MNRAS 176, 321
Greiner J., Hasinger G., Kahabka P., 1991, A&A 246, L17
Haiman Z, Magnier E.A., Lewin W.H.G., et al., 1994, A&A, 286, 725
Hasinger G., et al., 1992, GSFC OGIP Calibration Memo, CAL/ROS/92–001
Hasinger G., Burg R., Giacconi R., et al., 1993, A&A 275, 1

Hasinger G., 1994a, Supersoft X-ray Sources. In: Klare G. (ed.) Reviews in Modern Astronomy (7). Astronomische Gesellschaft, Hamburg, p. 129
Hasinger G., 1994b, Supersoft X-ray Sources. In: Holt S.S., Day C.S. (eds.) AIP Conference Proceedings (308), "The Evolution of X-ray Binaries" (MD October 1993). American Institute of Physics, New York, p. 611
Hasinger G., 1995, Annals New York Acad. Sci., 759, 200
Hertz P., Grindlay J.E., 1983, ApJ 275, 105
Jones L., et al., 1995, In: "Wide Field Spectroscopy and the Distant Universe", World Scientific London, p. 339
Kahabka P., Jain A., Pietsch W., 1991, "ROSAT Survey View of M 31", Kolloq. on Cataclysmic Variables and Low-Mass X-Ray Binaries, MPIA, Garching, October 1991
Kahabka P., Pietsch W., 1993, ROSAT Survey view of the SMC. In: Baschek B., Klare G., Lequeux J. (eds.) New Aspects of Magelanic Cloud Research. Springer, Heidelberg, p. 71
Kahabka P., Pietsch W., Hasinger G., 1994, A&A in press
Kato T., 1976, ApJS 30, 397
Koper E., Dame T.M., Israel F.P., Thaddeus P., 1991, ApJ 383, L11
Kormendy J., 1992, The Search for Black Holes in Galaxy Nuclei. In: Stenger V.J., Learned J.G., Pakvasa S., Tata X. (eds.) High Energy Neutrino Astrophysics. World Scientific. Singapore, p. 196
Long K.S., Speybroeck L.P.van, 1983, X-Ray Emission from Normal Galaxies. In: Lewin W.H.G., Heuvel E.P.J.van den (eds.) Accretion Driven Stellar X-Ray Sources. Cambridge University Press, Cambridge, p. 117
Maccacaro T., Gioia I.M., Wolter A., Zamorani G., Stocke J.T., 1988, ApJ 326, 680
Magnier E.A., Lewin W.H.G., van Paradijs J., et al., 1992, A&AS 96, 379. submitted
Magnier E.A., 1993, PhD Thesis MIT
Magnier E.A., Lewin W.H.G., van Paradijs J., et al., 1994a, A&AS, submitted
Magnier E.A., Prins S., van Paradijs J., et al., 1994b, A&AS, submitted
Meaburn J., 1980, MNRAS 192, 365
Morrison R., McCammon D., 1983, ApJ 270, 119
Pakull M.W., 1989, X-Ray View of the Magelanic Clouds. In: Boer K.S.de, Spite F., Stasinska G. (eds.) Recent Developments of Magellanic Cloud Research. Observatoire de Paris, Meudon/France, p. 183
Pellet A., Astier N., Viale A., et al., 1978, A&AS 31, 439
Pfeffermann E., Briel U.G., Hippmann H., et al., 1986, Proc. SPIE 733, 519
Primini F.A., Forman W., Jones C., 1993, ApJ 410, 615
Raymond J.C., Smith B.W., 1977, ApJS 35, 419
Sargent W.L.W., Kowal C.T., Hartwick F.D.A., Van den Bergh S., 1977, AJ 82, 947
Schaeidt S., Hasinger G., Trümper J., 1993, A&A 270, L9
Schmitt J.H.M.M., 1985, ApJ 293, 178
Sharov A.S., Alksnis A., 1991, Ap&SS 180, 273
Sharov A.S., Alksnis A., 1992, Ap&SS 190, 119
Snowden S.L., Plucinsky P.P., Briel U., Hasinger G., Pfeffermann E., 1992, ApJ 393, 819
Snowden S.L., Freyberg M.J., 1993, ApJ 404, 403
Stark A.A., Gammie C.F., Wilson R.W., et al., 1992, ApJS 79, 77
Trinchieri G., Fabbiano G., 1991, ApJ 382, 82 (TF)
Trümper J., 1983, Adv. Spaces Res. 2, No. 4, 241
Trümper, J., Hasinger G., Aschenbach B., et al., 1991, Nat 349, 579
Tully R.B., 1988, Nearby Galaxies Catalog. Cambridge University Press
Unwin S.C., 1980, MNRAS 192, 243
van den Heuvel E.P.J., Bhattacharya D., Nomoto K., Rappaport S.A., 1992, A&A 262, 97
van Speybroeck L.P., Epstein A., Forman W., et al., 1979, ApJ 234, L45
van Speybroeck L.P., Bechtold J., 1981, X-Ray Emission from Normal Galaxies. In: Giacconi R. (ed.) X-Ray Astronomy with the Einstein Satellite. Reidel, Dordrecht, p. 153
Verbunt F., Bunk W., Hasinger G., Johnston H.M., 1995, A&A submitted
Wang Q., Wu X., 1992, ApJS 78, 391
Zimmermann H.U., Belloni T., Izzo C., Kahabka P., Schwentker O., 1993, MPE Report 244, Ed. 3

This article was processed by the author using Springer-Verlag LaTeX A&A style file *L-AA* version 3.